

Neural mechanism of optimal limb coordination in crustacean swimming

Calvin Zhang^a, Robert D. Guy^a, Brian Mulloney^b, Qinghai Zhang^c, and Timothy J. Lewis^{a,1}

Departments of ^aMathematics and ^bNeurobiology, Physiology, and Behavior, University of California, Davis, CA 95616; and ^cDepartment of Mathematics, University of Utah, Salt Lake City, UT 84112

Edited by Eve Marder, Brandeis University, Waltham, MA, and approved July 17, 2014 (received for review December 16, 2013)

A fundamental challenge in neuroscience is to understand how biologically salient motor behaviors emerge from properties of the underlying neural circuits. Crayfish, krill, prawns, lobsters, and other long-tailed crustaceans swim by rhythmically moving limbs called swimmerets. Over the entire biological range of animal size and paddling frequency, movements of adjacent swimmerets maintain an approximate quarter-period phase difference with the more posterior limbs leading the cycle. We use a computational fluid dynamics model to show that this frequency-invariant stroke pattern is the most effective and mechanically efficient paddling rhythm across the full range of biologically relevant Reynolds numbers in crustacean swimming. We then show that the organization of the neural circuit underlying swimmeret coordination provides a robust mechanism for generating this stroke pattern. Specifically, the wave-like limb coordination emerges robustly from a combination of the half-center structure of the local central pattern generating circuits (CPGs) that drive the movements of each limb, the asymmetric network topology of the connections between local CPGs, and the phase response properties of the local CPGs, which we measure experimentally. Thus, the crustacean swimmeret system serves as a concrete example in which the architecture of a neural circuit leads to optimal behavior in a robust manner. Furthermore, we consider all possible connection topologies between local CPGs and show that the natural connectivity pattern generates the biomechanically optimal stroke pattern most robustly. Given the high metabolic cost of crustacean swimming, our results suggest that natural selection has pushed the swimmeret neural circuit toward a connection topology that produces optimal behavior.

locomotion | coupled oscillators | phase locking | metachronal waves

It is widely believed that neural circuits have evolved to optimize behavior that increases reproductive fitness. Despite this belief, few studies have clearly identified the neural mechanisms producing optimal behaviors. The complexity of behaviors generally makes it difficult to assess their optimality, and neural circuits are often too complicated to concretely link neural mechanisms to the overt behavior. Energy-intensive locomotion such as steady swimming, walking, and flying provides important model systems for studying optimality because the goal of the behavior is clear and it is likely to have been optimized for efficiency (1). For example, the kinematics of locomotion has been shown to be optimal in the cases of the undulatory motion of the sandfish lizard and the lamprey (2, 3). On the other hand, the neural circuits underlying locomotion in most organisms are not sufficiently characterized to understand how they give rise to the optimal motor behavior. Because of the distinct frequency-invariant stroke pattern and the relative simplicity of the neuronal circuit, limb coordination of long-tailed crustaceans during steady swimming provides an ideal model system for examining the optimality of motor behavior and its neural underpinnings.

During forward swimming, long-tailed crustaceans, like crayfish, krill, shrimp, and lobsters, propel themselves through the water using four or five pairs of abdominal limbs called swimmerets that move rhythmically through cycles of power strokes (PSs) and return strokes (RSs). Although these animals vary in size from 0.5 cm to over 40 cm and beat their swimmerets with

frequencies ranging from about 1 to 10 Hz (4, 5), the stroke pattern is invariant: limbs on neighboring abdominal segments always maintain an approximate quarter-period (0.25) phase difference in a tail-to-head metachronal wave (Fig. 1). This phenomenon is known as phase constancy. Measurements of the metabolic cost of krill swimming show that up to 73% of their daily energy expenditure is devoted to paddling (6). This and the facts that the distinct limb coordination is the only stroke pattern that these crustaceans exhibit when the swimmeret system is active and that this limb coordination is conserved across many species suggest that the stroke pattern is biomechanically optimized for swimming. This in turn suggests that evolution has pushed the properties of the underlying neural circuit to produce the distinct phase constant limb coordination.

Metachronal waves of motor activity during locomotion are observed in many animals, and the underlying neural circuits have been shown to consist of chains of local pattern-generating microcircuits [i.e., local central pattern generators (CPGs)] (7–10). This is the case for the neural circuits that control the undulatory motion of bony fish, amphibians, and lamprey during swimming (9–12) and the movements of swimmerets in crayfish (*Pacifastacus leniusculus*) (13). By modeling the neural circuit of the crayfish swimmeret system as a chain of generic phase oscillators, previous theoretical studies (14–16) showed that the tail-to-head 0.25 phase constant stroke pattern could be achieved if the phase response properties of the local CPGs to inputs from ascending and descending inter-CPG connections satisfy two different constraints. Similar results were obtained for the lamprey swimming neural circuit (11, 17). Many studies (e.g., refs. 14, 16, and 18) have addressed aspects of how these two constraints are satisfied, but it remains unclear how they

Significance

Despite the general belief that neural circuits have evolved to optimize behavior, few studies have clearly identified the neural mechanisms underlying optimal behavior. The distinct limb coordination in crustacean swimming and the relative simplicity of the neural coordinating circuit have allowed us to show that the interlimb coordination in crustacean swimming is biomechanically optimal and how the structure of underlying neural circuit robustly gives rise to this coordination. Thus, we provide a concrete example of how an optimal behavior arises from the anatomical structure of a neural circuit. Furthermore, our results suggest that the connectivity of the neural circuit underlying limb coordination during crustacean swimming may be a consequence of natural selection in favor of more effective and efficient swimming.

Author contributions: C.Z., R.D.G., and T.J.L. designed research; C.Z., R.D.G., B.M., and T.J.L. performed research; C.Z., R.D.G., Q.Z., and T.J.L. contributed new reagents/analytic tools; C.Z., R.D.G., B.M., and T.J.L. analyzed data; and C.Z., R.D.G., and T.J.L. wrote the paper.

The authors declare no conflict of interest.

This article is a PNAS Direct Submission.

¹To whom correspondence should be addressed. Email: tjlewis@ucdavis.edu.

This article contains supporting information online at www.pnas.org/lookup/suppl/doi:10.1073/pnas.1323208111/-DCSupplemental.

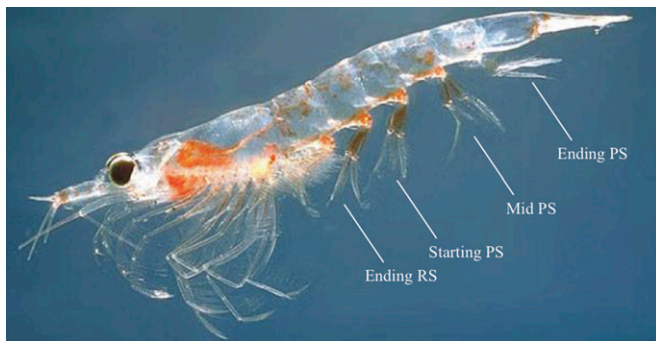


Fig. 1. Forward swimming of a crustacean. Cycles of power strokes (PSs) and return strokes (RSs) of the swimmerets provide the thrust for forward swimming. Movement of neighboring swimmerets maintains a quarter-period phase difference with the more posterior swimmeret leading the cycle. Image courtesy of Wikimedia Commons/Oystein Paulsen.

are achieved and maintained over a wide range of frequencies. Recent experimental work has elucidated the cellular composition of the local swimmeret CPGs and the synaptic organization of the circuit that connects them in the crayfish swimmeret system (13, 19, 20), allowing these issues to be directly addressed.

In this article, we first use computational fluid dynamics simulations to show that the metachronal multilimb stroke pattern with ~ 0.25 intersegmental phase differences is the most effective and efficient metachronal stroke pattern across the entire biologically relevant range of body sizes and stroke frequencies in crustacean swimming. We then show that the half-center structure of the local CPG circuits (21–23) and the topology of the inter-CPG connections in the crayfish swimmeret circuit (19, 20) provide a robust neural mechanism for producing the 0.25 phase-locked metachronal wave. This reduces the previously determined constraints on the phase response properties of the CPGs to a single condition. Furthermore, we experimentally measure the phase response properties of the crayfish swimmeret CPG circuit and show that this single condition holds. Finally, we consider all possible topologies for connections between the local CPGs and show that the network topology present in the crayfish swimmeret circuit generates the biomechanically optimal stroke pattern most robustly.

The Mechanical Advantage of the Tail-to-Head Metachronal Wave of Swimmeret Coordination

Metachronal waves of ciliary beating in microorganisms are the subject of intense recent study (24–27). These previous works found that metachronal waves may allow cilia to propel cells forward with higher propulsion velocity and efficiency. However, metachronal waves in ciliary beating differ from the metachronal paddling rhythm in crustacean swimming in many ways: (i) Swimmerets are plate-like paddles, whereas cilia are hair-like appendages. (ii) The limb angle of swimmerets changes smoothly through the cycle with a duty cycle of approximately one-half, whereas cilia use a fast power stroke and a slow sweeping recovery stroke. (iii) Although both swimmerets and cilia beat in a back-to-front metachronal wave, the phase difference between neighboring swimmerets is $\sim 25\%$, whereas the phase difference between appendages varies from $\sim 1\%$ to $\sim 10\%$ depending on the organism and location of the cilia on the organism. (iv) Evidence suggests that phase locking of cilia occurs through hydrodynamic forces, whereas neural activity is the primary determinant of phase locking of crustacean swimmerets. (v) The fluid dynamics resulting from cellular level metachronal waves are characterized by Reynolds numbers (Re) close to 0. The Re characterizes the relative importance of inertial forces to viscous forces in the flow. For $Re \approx 0$, viscous forces dominate and inertial forces can be neglected. The Re increases with the size of

the animal (characteristic length scale) and decreases with the stroke period (characteristic time scale). The natural variation in a crustacean's size and stroke frequency leads to Re ranging from about 10 to 1,000 (*SI Text, section 1.1*), under which both viscous and inertial effects are relevant. Hence, the fluid dynamics of cilia beating are significantly different from the fluid dynamics of crustacean swimming. Relatively few studies have examined metachronal limb paddling for the range of Re under which crustaceans operate (28–30). Recently, a model based on drag forces alone predicted a slight mechanical advantage of metachronal wave in krill swimming (31). However, this model does not capture the nonlinear interactions of the forces generated by the multiple limbs arising from the local flow, which have a significant effect on swimming when limbs are close to each other. To capture this essential effect, we build a computational fluid dynamics model and numerically compute the flow field produced by crayfish's tail-to-head metachronal limb stroke pattern and other hypothetical patterns.

Our fluid dynamics model consists of four rigid paddles as limbs moving with prescribed motion attached to a fixed wall immersed in a two-dimensional fluid. To approximate the fact that swimmerets are straight and fanned-out during PS and are curled and folded during RS, we treat swimmerets as impermeable during PS and permeable during RS (see *Materials and Methods, SI Text, section 1*, and *Figs. S1–S6* for details).

We compute the flux of the fluid moving in the tail direction and take its time average as a measure of the effectiveness of the swimmeret stroke pattern. Fig. 2*B* depicts the flux of three different stroke patterns (the natural tail-to-head metachronal wave with 0.25 intersegmental phase differences, the in-phase rhythm, and the head-to-tail metachronal wave with 0.75 intersegmental phase differences) at an intermediate Reynolds number ($Re = 200$). Both metachronal stroke patterns produce smoother temporal variation in flux compared to the in-phase rhythm because PS and RS are evenly distributed in time among the four limbs. A remarkable observation is that the natural tail-to-head metachronal wave produces a 60% increase in average flux over that of the in-phase rhythm and a 500% increase over that of the head-to-tail metachronal wave.

To illustrate this increased effectiveness of the natural tail-to-head metachronal wave over other stroke patterns, we put in free-flowing tracers in the flow and observe how different stroke patterns lead to different tracer displacement. To allow the initial transient effect to disappear, we first let the swimmerets beat for five periods. At the end of the fifth period, we put in the passive tracers uniformly underneath the body. We observe how the passive tracers move as the swimmerets undergo another five periods of strokes under the three different stroke patterns (Fig. 2*A* and *Movies S1–S3*). Fig. 2*A* illustrates that, with the natural 0.25 phase-locked tail-to-head metachrony, the majority of the tracers are propelled toward the tail direction. The in-phase rhythm is less effective in driving the tracers toward the tail direction compared to the natural tail-to-head metachrony. With the 0.75 phase-locked head-to-tail metachrony, it is not clear whether the tracers are flowing in any particular direction. Overall, among the three stroke patterns, the natural tail-to-head metachronal wave of swimmeret coordination is the most effective stroke pattern in maximizing flux.

The above results are based on simulations for an intermediate Reynolds number ($Re = 200$). As the Re changes, the flow characteristics change significantly (*Movies S1–S3*). Nevertheless, the relative advantage of the tail-to-head metachronal wave over other metachronies is preserved across biologically relevant Reynolds numbers. Fig. 2*C* shows that the natural tail-to-head metachronal wave of swimmeret coordination with 0.25 intersegmental phase differences produces the largest average flux among all metachronal waves for $Re = 50, 200$, and 800.

As a measure of the efficiency of the stroke pattern, we normalize the average flux by the average power consumption per stroke period (*SI Text, section 1.3*). The natural tail-to-head

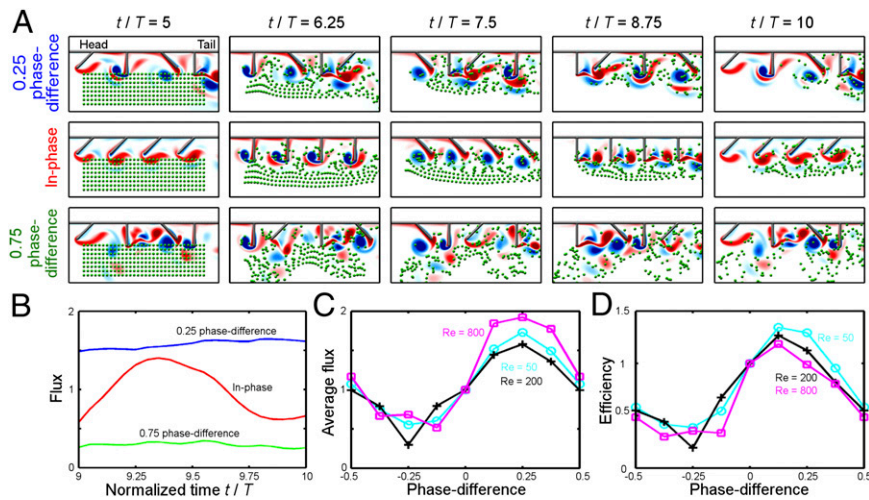


Fig. 2. Computational fluid dynamics model of crayfish swimmeret paddling. (A) Snapshots of the flow field at Reynolds number 200 under the natural tail-to-head metachrony with 0.25 phase difference, the hypothetical in-phase rhythm, and the hypothetical head-to-tail metachrony with 0.75 phase difference. Free-flowing tracers are shown as green dots; red denotes positive vorticity; and blue denotes negative vorticity. (B) Flux vs. normalized time for flows in A. (C) Average flux vs. phase difference. (D) Efficiency vs. phase difference. For B–D, the curves are normalized by the time-averaged flux or efficiency of the in-phase rhythm. For C and D, results for three Reynolds numbers are provided: 50 (cyan curve with “O”), 200 (black curve with “+”), and 800 (magenta curve with “□”).

metachronal wave of swimmeret coordination achieves close-to-maximal efficiency among all metachronies over a wide range of biologically relevant Reynolds numbers. Fig. 2D shows that the efficiency peaks at 0.125 phase difference closely followed by the 0.25 phase difference. Across Reynolds numbers from 50 to 800, the natural tail-to-head metachronal wave is up to 30% more efficient than the in-phase rhythm and 300% to 550% more efficient than the head-to-tail metachronal wave.

Overall, the above results show that the natural 0.25 phase-locked metachrony leads to near-maximal effectiveness and efficiency over the full span of biologically relevant Reynolds numbers in crustacean swimming, i.e., a significant biomechanical advantage is preserved despite the large variation in crustaceans’ size and swimmeret stroke frequency. The biomechanical optimality of the tail-to-head metachronal wave with approximate 0.25 intersegmental phase differences that is independent of swimmeret beat frequencies raises the question: What are the neural mechanisms that maintain this limb coordination in such a robust manner?

A Robust Neural Mechanism Producing Phase Constancy

The isolated neural ventral cord of the crayfish, which contains the neural circuit driving the movement of the swimmerets, displays fictive locomotion (Fig. 3A). That is, it expresses rhythmic neural activity that is analogous to the distinct stroke pattern observed behaviorally (13, 32). This centrally generated rhythm is the primary determinant of the swimmeret coordination (*SI Text*, sections 1.2, 2.1, and 3). Experiments on the crayfish neural ventral cord indicate that (i) each swimmeret is innervated by an anatomically separate and functionally independent CPG (22, 33), and (ii) these CPGs are connected through ascending and descending coordinating neurons (19). Thus, the neural circuit driving metachronal swimmeret movements can be considered as a chain of four pairs of neuronal oscillators.

A useful mathematical framework for studying dynamics of interconnected CPGs is the coupled phase model (17, 34), where the state of each CPG is described completely by its phase. If the i th CPG is isolated, then its phase θ_i ($0 \leq \theta_i < 1$) will evolve at its intrinsic frequency ω , i.e., $\theta_i = (\omega t + \phi_i^0) \bmod 1$, where ϕ_i^0 is the initial phase of the CPG. If the i th CPG is coupled with the j th CPG, then the rate of change of phase will be sped up or slowed down due to input from this intersegmental coupling. The magnitude of the acceleration or deceleration of phase depends on the timing and structure of the input from the j th CPG and the state-dependent response of the i th CPG. This effect is quantified by the “interaction function,” which is a function of

the phase difference between the two coupled CPGs (18, 35) and is related to the phase response curve (*SI Text*, section 2.2).

Previously, Skinner et al. (15) used the phase model framework to describe the neural circuit of the crayfish swimmeret system as a chain of four generic oscillators with nearest-neighbor coupling:

$$\begin{cases} \frac{d\theta_1}{dt} = \omega + H_{\text{asc}}(\theta_2 - \theta_1), \\ \frac{d\theta_i}{dt} = \omega + H_{\text{asc}}(\theta_{i+1} - \theta_i) + H_{\text{dsc}}(\theta_{i-1} - \theta_i), \quad i=2 \text{ and } 3, \\ \frac{d\theta_4}{dt} = \omega + H_{\text{dsc}}(\theta_3 - \theta_4), \end{cases} \quad [1]$$

where H_{asc} and H_{dsc} are the interaction functions for ascending and descending connections, respectively. Because the interaction functions are functions of the phase difference between the CPGs, they are 1-periodic functions. Phase-locked rhythms correspond to states in which the intersegmental phase differences $\Delta\theta_i = \theta_{i+1} - \theta_i$ are constant, i.e., $(d\Delta\theta_i)/dt = 0$ for $i=1, 2$, and 3. Metachronal waves correspond to phase-locked states where $\Delta\theta_i$ are equal. Note that the tail-to-head 0.25 phase-locked state requires both $H_{\text{asc}}(0.25) = 0$ and $H_{\text{dsc}}(-0.25) = 0$. The question remains as to how the structure of the crayfish neural circuit maintains these two constraints on the interaction functions, and therefore maintains the optimal stroke pattern, over a broad range of stroke frequencies. However, recent experimental findings elucidating the structure of the crayfish swimmeret neural circuit allow this question to be addressed.

Accumulated anatomical and physiological results on the local and intersegmental circuitry of the crayfish swimmeret system (13, 19, 20, 23, 36) have revealed the following circuit architecture (for a more detailed description of the circuit, see *SI Text*, section 2.1 and Fig. S7): Each local CPG is composed of a half-center oscillator (HCO) that consists of two mutually inhibited neurons, a P cell and an R cell, that oscillate in antiphase. The P cell drives the PS motor neurons, and the R cell drives the RS motor neurons. Each local HCO has the same frequency and is effectively coupled with its nearest neighbor(s) through intersegmental connections diagrammed in Fig. 3B. The descending connection is effectively excitatory and goes from the P cell of an HCO to the R cell of its more posterior neighbor HCO. The ascending connection is effectively excitatory and goes from the R cell in an HCO to the R cell of its more anterior neighbor HCO. The ascending and the descending intersegmental connections

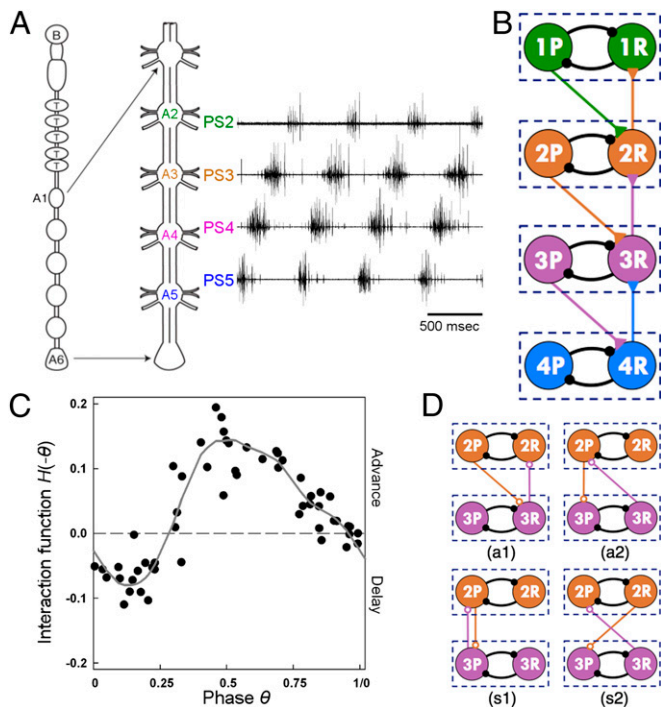


Fig. 3. Neuronal circuitry underlying the crayfish swimmeret system. (A) The neural circuit underlying the crayfish swimmeret system consists of a chain of four CPGs located in the abdominal ganglion A2–A5. Each CPG innervates motor neurons that drive the power strokes (PSs) and return strokes (RSs) of a swimmeret. The dissected neural cord in isolation can generate the tail-to-head metachronal wave of neuronal activity as seen in the simultaneous extracellular recordings from the four PS motor nerves, PS2–PS5. (B) Schematic diagram of the neural circuit composed of a chain of four coupled CPGs. Each CPG is modeled as an HCO consisting of two mutually inhibited cells (large circles in diagram) that oscillate in antiphase. Cells in HCOs denoted by *i*P drive PS motor neurons, and cells denoted by *i*R drive RS motor neurons (*i* = 1, 2, 3, and 4). The small solid black circles symbolize inhibitory connections, the small solid triangles symbolize excitatory connections, and the colors indicate the origin of each intersegmental connection. (C) Experimentally measured interaction function *H* for a crayfish swimmeret CPG. (D) The natural network topology (a1) in the crayfish swimmeret neural circuit and three hypothetical network topologies, (a2), (s1), and (s2), in a chain of four HCOs with nearest-neighbor coupling. Only the middle two HCOs are shown. The small open circles symbolize either excitatory or inhibitory connections.

between nearest neighbors have similar strength and dynamics. We will show that the CPGs' half-center structure and the asymmetric intersegmental connectivity described above provide a robust mechanism for generating the 0.25 phase constancy independent of the intrinsic properties of the CPGs and details of the intersegmental coupling.

A Phase Model for Two Coupled HCOs. It is instructive to first consider a subnetwork of two coupled HCOs in which each HCO has only one incoming connection and one outgoing connection. Because (i) the ascending connection between the HCOs is between R cells, (ii) the descending connection links a P cell to an R cell, and (iii) the P and R cells in each HCO are in antiphase, the descending output is effectively phase delayed by a half-period with respect to the ascending output. In the phase model, the entire local module is considered to be an oscillatory unit, whose state is described by its phase θ_i alone, but the ascending and descending outputs are in antiphase, i.e., θ_i and $\theta_i + 0.5$, respectively. Hence, by defining $H(\theta_2 - \theta_1) = H_{\text{asc}}(\theta_2 - \theta_1)$, the interaction function for the descending connection can be rewritten

as $H_{\text{dsc}}(\theta_1 - \theta_2) = H(\theta_1 - \theta_2 + 0.5)$. Therefore, the dynamics of the two HCOs is described by a system of two differential equations:

$$\begin{cases} \frac{d\theta_1}{dt} = \omega + H_{\text{asc}}(\theta_2 - \theta_1) = \omega + H(\theta_2 - \theta_1), \\ \frac{d\theta_2}{dt} = \omega + H_{\text{dsc}}(\theta_1 - \theta_2) = \omega + H(\theta_1 - \theta_2 + 0.5). \end{cases} \quad [2]$$

It follows that the phase difference $\Delta\theta = \theta_2 - \theta_1$ between the HCOs is given by a single differential equation:

$$\frac{d\Delta\theta}{dt} = H(-\Delta\theta + 0.5) - H(\Delta\theta). \quad [3]$$

Because *H* has a period of 1, Eq. 3 reveals that $\Delta\theta = 0.25$ and 0.75 are always phase-locked states. We stress that this result is independent of the frequency of the oscillator and does not rely on tuning any specific biophysical parameters. This implies that the phase constancy of the 0.25 phase-locked state arises robustly from the organization of the neuronal circuitry (37).

The invariance of the phase-locked state with the 0.25 phase difference can be understood by considering the timing of the output from the half-center oscillators relative to the phase at which the oscillators receive the input. Suppose that HCO-2 is phase advanced by 0.25 relative to HCO-1. The R cell of HCO-1 receives input from the R cell of HCO-2 that is phase advanced by 0.25. On the other hand, the R cell of HCO-2 receives input from the P cell of HCO-1, which is a half-period out of phase with the R cell of HCO-1. Thus, the R cell of HCO-2 receives input that is effectively phase advanced by 0.25 (i.e., $-0.25 + 0.5$). This implies that both oscillators receive input at the exact same phases in their cycles. Therefore, they adjust their instantaneous frequencies in the exact same way, and HCO-2 remains phase advanced by 0.25 relative to HCO-1.

The Full Circuit of Four Coupled HCOs. Although the crayfish's four-HCO neural circuit is not a trivial generalization of the two-HCO circuit, the half-center structure of the CPG and the asymmetric intersegmental connectivity are still the key organizational features of the four-HCO neural circuit that gives rise to an approximate 0.25 phase constancy. From Eq. 1, the dynamics of the phase differences between each neighboring HCO $[(\Delta\theta_1, \Delta\theta_2, \Delta\theta_3)]$, where $\Delta\theta_i = \theta_{i+1} - \theta_i$ are described by:

$$\begin{cases} \frac{d\Delta\theta_1}{dt} = H_{\text{asc}}(\Delta\theta_2) + H_{\text{dsc}}(-\Delta\theta_1) - H_{\text{asc}}(\Delta\theta_1), \\ \frac{d\Delta\theta_2}{dt} = H_{\text{asc}}(\Delta\theta_3) + H_{\text{dsc}}(-\Delta\theta_2) - H_{\text{asc}}(\Delta\theta_2) - H_{\text{dsc}}(-\Delta\theta_1), \\ \frac{d\Delta\theta_3}{dt} = H_{\text{dsc}}(-\Delta\theta_3) - H_{\text{asc}}(\Delta\theta_3) - H_{\text{dsc}}(-\Delta\theta_2). \end{cases} \quad [4]$$

As mentioned earlier, $(\Delta\theta_1, \Delta\theta_2, \Delta\theta_3) = (0.25, 0.25, 0.25)$ is a phase-locked state if and only if both $H_{\text{asc}}(0.25) = 0$ and $H_{\text{dsc}}(-0.25) = 0$. Note that these are two independent conditions that the crayfish swimmeret neural circuit needs to satisfy. However, because of the half-center structure of the CPGs and the intersegmental connectivity (Fig. 3B), one of the above two conditions is eliminated. Recall that the descending outputs are effectively phase delayed by a half-period with respect to the ascending outputs, i.e., $H_{\text{asc}}(\theta_2 - \theta_1) = H(\theta_2 - \theta_1)$ and $H_{\text{dsc}}(\theta_1 - \theta_2) = H(\theta_1 - \theta_2 + 0.5)$. By substituting these expressions into Eq. 4, we find that $(\Delta\theta_1, \Delta\theta_2, \Delta\theta_3) = (0.25, 0.25, 0.25)$ is a phase-locked state if and only if $H(0.25) = 0$. That is, because of the special organization of the four-HCO neural circuit, the crayfish swimmeret neural circuit only needs to meet one condition to produce the tail-to-head 0.25 phase locking.

Furthermore, the condition $H(0.25) = 0$ can be relaxed if we allow a small deviation from the exact 0.25 phase locking, i.e., if we consider an approximate 0.25 phase-locked solution $(\Delta\theta_1, \Delta\theta_2, \Delta\theta_3) = (0.25 + \varepsilon, 0.25, 0.25 - \varepsilon)$ for some small ε . From Eq. 4, an approximate 0.25 phase locking exists if and only if $H(0.25) + H(0.25 - \varepsilon) - H(0.25 + \varepsilon) = 0$. This condition is equivalent to the condition that $\varepsilon \approx H(0.25)/2H'(0.25)$ is small. For example, if the ratio $|H(0.25)/H'(0.25)|$ is less than 20%, the resulting phase differences will be between 0.15 and 0.35 approximately. In addition, one can show that the tail-to-head 0.25 phase locking is stable if H has a positive slope at 0.25, i.e., $H'(0.25) > 0$ (*SI Text, section 2.3* and *Tables S1* and *S2*). Note that, in the above analysis, we have assumed identical strength for ascending and descending connections because experimental results have shown that they are similar in strength and dynamics. In *SI Text, section 2.4*, we further show that this equal strength minimizes the deviation of the phase-locked state from 0.25.

Experimentally Measured Interaction Function. Our analysis shows that if each crayfish swimmeret local CPG (the kernel of which is a HCO) satisfies the condition that $\varepsilon = H(0.25)/2H'(0.25)$ is small, then the swimmeret neuronal circuitry gives rise to the robust 0.25 phase locking. Indeed, Fig. 3C shows that the experimentally measured interaction function $H(\theta)$ is relatively small at 0.25, and has a relatively steep positive slope at this point, giving rise to $\varepsilon \approx H(0.25)/2H'(0.25) = 0.06$. Therefore, both the existence condition (ε is small) and the stability condition [$H'(0.25) > 0$] predicted by our mathematical model are satisfied. It can be further shown that these conditions on the interaction function arise from the generic phase response properties of HCOs (*SI Text, section 2.6*).

Discussion

Our results demonstrate that the distinct limb coordination in crustacean swimming provides the biomechanically optimal stroke pattern over a wide range of biologically relevant paddling frequencies and animal sizes, i.e., Reynolds numbers (Re). Furthermore, the relative simplicity of the crustacean nervous system and recent advances in the knowledge of the crayfish swimmeret neuronal circuit allow us to identify how the structure of the circuit robustly gives rise to this stroke pattern. Thus, the swimmeret system of long-tailed crustaceans serves as a concrete example of how the architecture of a neural circuit gives rise to optimal locomotor behavior.

Our computational fluid dynamics simulations show that the flow characteristics are substantially different as the Re changes from 50 to 800 (*Movies S1–S3*). Despite these differences, the distinct tail-to-head metachronal stroke pattern maintains a significant advantage over other stroke patterns. Furthermore, the relative advantage of this limb coordination persists over the natural variation of limb spacing (*SI Text, section 1.3*, and *Fig. S6*). This suggests that the primary mechanism that gives the distinct tail-to-head metachronal stroke pattern a significant advantage over other stroke patterns does not involve careful timing of limb movements to exploit subtle fluid–structure interactions. Instead, we conjecture that the advantage arises from a simple, robust geometric mechanism based on the asymmetric arrangement of the neighboring limbs during PSs and RSs. Because PS generates positive flux whereas RS counteracts the flux generation, an efficient stroke pattern should maximize the effect of PS while minimizing the effect of RS. As illustrated in Fig. 4, under the natural tail-to-head metachrony with 0.25 phase difference, the volume of fluid enclosed by the neighboring limbs during PS is much larger than that during RS. This significant asymmetry in the volume of fluid enclosed by the PS and the RS leads to a very effective mechanism for generating positive flux. Therefore, a significantly larger average flux is generated under the natural 0.25 phase-locked rhythm compared to the case with the in-phase rhythm, under which the PS and the RS enclose the same volume of fluid. Similar to the reasoning above, under the

hypothetical 0.75 phase-locked head-to-tail metachrony, the PS encloses a much smaller volume of fluid than the RS does. Hence, the head-to-tail metachrony is an ineffective stroke pattern for generating positive flux.

Experimental results show that the timing of the swimmeret movements is strongly correlated with the timing of the bursts of muscle activity caused by motor neuron input (38). Furthermore, long-tailed crustaceans exhibit the distinct tail-to-head stroke pattern in a variety of swimming modes, including forward swimming and hovering, in which the limbs experience different hydrodynamic forces (29). These observations suggest that the intersegmental phase differences between swimmerets result primarily from neural input to the muscles rather than from the interaction between hydrodynamic forces and passive body mechanics. Neural input to the muscles is shaped by the rhythm intrinsically generated in the central nervous system and sensory feedback. However, while proprioceptive reflexes appear to be able to increase the PS motor drive to compensate for changes in load on the swimmerets (39, 40), extensive experimental evidence suggests that proprioceptive feedback has little effect on interlimb coordination (41–43). Thus, sensory feedback, hydrodynamic forces, and limb mechanics are likely to influence the stroke kinematics of an individual limb and the animal's overall swimming performance, but the feedforward drive from the central nervous system is the primary determinant of coordination between limbs. (See *SI Text, section 1.2* and *section 3*, for details.)

The key organizational features of the crayfish neural circuit for producing the phase constancy with 0.25 intersegmental phase differences are the internal half-center structure of the local CPG and the topology of the ascending and descending connections between the local CPGs. To highlight this fact, let us consider other hypothetical patterns of intersegmental connection in a chain of four HCO-based CPGs. Fig. 3D shows the four fundamentally different connectivity patterns that can occur between HCOs with only one ascending and one descending connection. Connection scheme (a1) is the connectivity that is present in the crayfish swimmeret neural circuit, and (a2), (s1), and (s2) are three hypothetical network topologies. Depending on whether the coupling is between a P cell and an R cell or between the same cell type, the overall network topology can be asymmetric or symmetric. It can be shown (*SI Text, section 2.3*) that a symmetric network topology (s1) or (s2) can robustly produce the in-phase rhythm and the antiphase rhythm (0.5 phase difference); however, they do not robustly produce the natural tail-to-head metachronal wave (0.25 phase difference). Furthermore, given the response properties of the crayfish swimmeret local CPGs (as in Fig. 3C), the asymmetric topology (a2) can robustly produce the head-to-tail metachronal wave (0.75 phase difference) but not the natural tail-to-head metachronal wave (0.25 phase difference).

The results discussed above can be extended beyond circuits with single ascending and descending connections between neighboring modules and equal connection strengths. In fact, it can be shown that, in the chain of four HCOs, equal ascending and descending connection strengths minimize the deviation of the intersegmental phase difference from 0.25 (*SI Text, section 2.4*). Furthermore, if multiple ascending or descending connections between neighboring HCOs are permitted, then circuit topologies other than (a1) can produce robust phase locking with phase lags of 0.25, but these connectivity schemes must have an analogous structure to the (a1)

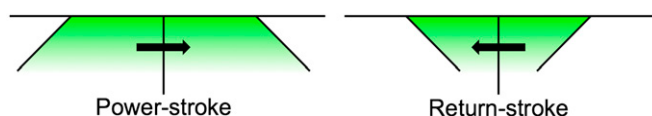


Fig. 4. Position of neighboring limbs in the middle of the PS and the RS, respectively, in the natural 0.25 phase-locked rhythm.

connection scheme. That is, descending connections must link P and R cells, whereas ascending connections must link R cells to R cells and/or P cells to P cells, and the connection strengths must be appropriately balanced (*SI Text, section 2.5*). Although it is possible that other connectivity schemes could support the 0.25 tail-to-head metachronal limb coordination, well-tuned compensatory mechanisms would be required to maintain this coordination over a wide range of paddling frequencies. Thus, the natural asymmetric circuit topology (a1) appears to generate this stroke pattern with the maximal robustness and minimal requirements.

HCOs are general, primitive motifs in locomotor CPGs and often serve as building blocks for networks of CPGs (44, 45). This fact and our finding that the natural asymmetric network topology in the crayfish swimmeret neural circuit is superior to all other intersegmental connectivity schemes in a chain of HCOs in robustly producing the biomechanically optimal tail-to-head metachronal stroke pattern suggest that similar neural circuits drive coordinated swimmeret movement in all long-tailed crustaceans. Furthermore, given the large metabolic cost of crustacean swimming (6, 46), our results suggest that the asymmetric network topology is the result of natural selection in favor of more effective and efficient swimming.

- Todorov E (2004) Optimality principles in sensorimotor control. *Nat Neurosci* 7(9):907–915.
- Maladen RD, Ding Y, Umbanhowar PB, Kamor A, Goldman DI (2011) Mechanical models of sandfish locomotion reveal principles of high performance subsurface sand-swimming. *J R Soc Interface* 8(62):1332–1345.
- Tytell ED, Hsu C-Y, Williams TL, Cohen AH, Fauci LJ (2010) Interactions between internal forces, body stiffness, and fluid environment in a neuromechanical model of lamprey swimming. *Proc Natl Acad Sci USA* 107(46):19832–19837.
- Neil DM, Macmillan DL, Robertson RM, Laverack MS (1976) The structure and function of thoracic exopodites in the larvae of the lobster *Homarus gammarus* (L.). *Philos Trans R Soc Lond B Biol Sci* 274(929):53–68.
- Mulloney B, Harness PI, Hall WM (2006) Bursts of information: Coordinating interneurons encode multiple parameters of a periodic motor pattern. *J Neurophysiol* 95(2):850–861.
- Swadlow KM, Ritz DA, Nicol S, Osborn JE, Gurney LJ (2005) Respiration rate and cost of swimming for Antarctic krill, *Euphausia superba*, in large groups in the laboratory. *Mar Biol* 146(6):1169–1175.
- Mulloney B, Smarandache C (2010) Fifty years of CPGs: Two neuroethological papers that shaped the course of neurophysiology. *Front Behav Neurosci* 4:45.
- Stein PSG (2008) Motor pattern deletions and modular organization of turtle spinal cord. *Brain Res Brain Res Rev* 57(1):118–124.
- Grillner S (2006) Biological pattern generation: The cellular and computational logic of networks in motion. *Neuron* 52(5):751–766.
- Ijspeert AJ (2008) Central pattern generators for locomotion control in animals and robots: A review. *Neural Netw* 21(4):642–653.
- Cohen AH, et al. (1992) Modelling of intersegmental coordination in the lamprey central pattern generator for locomotion. *Trends Neurosci* 15(11):434–438.
- Bagnall MW, McLean DL (2014) Modular organization of axial microcircuits in zebrafish. *Science* 343(6167):197–200.
- Mulloney B, Smarandache-Wellmann C (2012) Neurobiology of the crustacean swimmeret system. *Prog Neurobiol* 96(2):242–267.
- Jones SR, Mulloney B, Kaper TJ, Kopell N (2003) Coordination of cellular pattern-generating circuits that control limb movements: The sources of stable differences in intersegmental phases. *J Neurosci* 23(8):3457–3468.
- Skinner FK, Kopell N, Mulloney B (1997) How does the crayfish swimmeret system work? Insights from nearest-neighbor coupled oscillator models. *J Comput Neurosci* 4(2):151–160.
- Skinner FK, Mulloney B (1998) Intersegmental coordination of limb movements during locomotion: Mathematical models predict circuits that drive swimmeret beating. *J Neurosci* 18(10):3831–3842.
- Cohen AH, Holmes PJ, Rand RH (1982) The nature of the coupling between segmental oscillators of the lamprey spinal generator for locomotion: A mathematical model. *J Math Biol* 13(3):345–369.
- Varkonyi PL, Kiemel T, Hoffman K, Cohen AH, Holmes P (2008) On the derivation and tuning of phase oscillator models for lamprey central pattern generators. *J Comput Neurosci* 25(2):245–261.
- Smarandache C, Hall WM, Mulloney B (2009) Coordination of rhythmic motor activity by gradients of synaptic strength in a neural circuit that couples modular neural oscillators. *J Neurosci* 29(29):9351–9360.
- Smarandache-Wellmann C, Weller C, Mulloney B (2014) Mechanisms of coordination in distributed neural circuits: Decoding and integration of coordinating information. *J Neurosci* 34(3):793–803.
- Mulloney B, Hall WM (2003) Local commissural interneurons integrate information from intersegmental coordinating interneurons. *J Comp Neurol* 466(3):366–376.
- Murchison D, Chrachri A, Mulloney B (1993) A separate local pattern-generating circuit controls the movements of each swimmeret in crayfish. *J Neurophysiol* 70(6):2620–2631.
- Smarandache-Wellmann C, Weller C, Wright TM, Jr, Mulloney B (2013) Five types of nonspiking interneurons in local pattern-generating circuits of the crayfish swimmeret system. *J Neurophysiol* 110(2):344–357.
- Elgeti J, Gommer G (2013) Emergence of metachronal waves in cilia arrays. *Proc Natl Acad Sci USA* 110(12):4470–4475.
- Michelin S, Lauga E (2010) Efficiency optimization and symmetry-breaking in a model of ciliary locomotion. *Phys Fluids* 22(11):111901.
- Gueron S, Levit-Gurevich K (1999) Energetic considerations of ciliary beating and the advantage of metachronal coordination. *Proc Natl Acad Sci USA* 96(22):12240–12245.
- Osterman N, Vilfan A (2011) Finding the ciliary beating pattern with optimal efficiency. *Proc Natl Acad Sci USA* 108(38):15727–15732.
- Lim JL, Demont ME (2009) Kinematics, hydrodynamics and force production of pleopods suggest jet-assisted walking in the American lobster (*Homarus americanus*). *J Exp Biol* 212(17):2731–2745.
- Murphy DW, Webster DR, Kawaguchi S, King R, Yen J (2011) Metachronal swimming in Antarctic krill: Gait kinematics and system design. *Mar Biol* 158(11):2541–2554.
- Williams TA (1994) A model of rowing propulsion and the ontogeny of locomotion in *Artemia* larvae. *Biol Bull* 187(2):164–173.
- Alben S, Spears K, Garth S, Murphy D, Yen J (2010) Coordination of multiple appendages in drag-based swimming. *J R Soc Interface* 7(52):1545–1557.
- Hughes GM, Wiersma CAG (1960) The co-ordination of swimmeret movements in the crayfish, *Procambarus clarkii* (Girard). *J Exp Biol* 37(4):657–672.
- Mulloney B, Hall WM (2000) Functional organization of crayfish abdominal ganglia. III. Swimmeret motor neurons. *J Comp Neurol* 419(2):233–243.
- Kopell N, Ermentrout GB (1988) Coupled oscillators and the design of central pattern generators. *Math Biosci* 90(1–2):87–109.
- Zhang C, Lewis TJ (2013) Phase response properties of half-center oscillators. *J Comput Neurosci* 35(1):55–74.
- Smarandache-Wellmann C, Grätsch S (2014) Mechanisms of coordination in distributed neural circuits: Encoding coordinating information. *J Neurosci* 34(16):5627–5639.
- Golubitsky M, Stewart I, Buono PL, Collins JJ (1999) Symmetry in locomotor central pattern generators and animal gaits. *Nature* 401(6754):693–695.
- Davis WJ (1968) Neuromuscular basis of lobster swimmeret beating. *J Exp Zool* 168(3):363–378.
- Cattaert D, Clarac F (1987) Rami motor neurons and motor control of the swimmeret system of *Homarus gammarus*. *J Comp Physiol A* 160(1):55–68.
- Davis WJ (1969) The neural control of swimmeret beating in the lobster. *J Exp Biol* 50(1):99–117.
- Deller SRT, MacMillan DL (1989) Entrainment of the swimmeret rhythm of the crayfish to controlled movements of some of the appendages. *J Exp Biol* 144(1):257–278.
- Heitler WJ (1982) Non-spiking stretch receptors in the crayfish swimmeret system. *J Exp Biol* 96(1):355–366.
- Mulloney B, Smarandache-Wellmann CR, Weller C, Hall WM, DiCaprio RA (2014) Proprioceptive feedback modulates coordinating information in a system of segmentally-distributed microcircuits. arXiv:1407.3249 [q-bio.NC].
- Hooper SL (2000) Central pattern generators. *Curr Biol* 10(5):R176–R177.
- Marder E, Calabrese RL (1996) Principles of rhythmic motor pattern generation. *Physiol Rev* 76(3):687–717.
- Torres JJ (1984) Relationship of O₂ consumption to swimming speed in *Euphausia pacifica*. Drag, efficiency and a comparison with other swimming organisms. *Mar Biol* 78(3):231–237.
- Peskin CS (2002) The immersed boundary method. *Acta Numer* 11:479–517.
- Netoff T, Schwemmer MA, Lewis TJ (2012) Experimentally estimating phase response curves of neurons: Theoretical and practical issues. *Phase Response Curves in Neuroscience: Theory, Experiment, and Analysis*, eds Schultheiss NW, Prinz AA, Butera RJ (Springer, New York), Vol 6, pp 95–129.

Supporting Information

Zhang et al. 10.1073/pnas.1323208111

Section 1. Fluid Dynamics Model

Section 1.1. Fluid Model. Our model of the swimmeret system consists of four rigid paddles (limbs) attached to a fixed rigid wall (body) immersed in a two-dimensional fluid. The limbs move with a prescribed swinging motion mimicking the power strokes (PSs) and return strokes (RSs) of the swimmerets. Specifically, the angle between the limb and the body (Fig. S1) is prescribed to be $\alpha_i(t) = \bar{\alpha} - A \cos(2\pi((t/T) + \phi_i))$, where $A = \pi/4$ is the amplitude, $\bar{\alpha} = \pi/2$ is the mean angle, T is the stroke period, ϕ_i is the relative phase of the i th limb, and t is time. Different stroke timing patterns are realized through the choice of relative phase ϕ_i , e.g., the natural tail-to-head metachrony with 0.25 phase difference is achieved using $\phi_1 = 0$, $\phi_2 = 0.25$, $\phi_3 = 0.5$, and $\phi_4 = 0.75$. Limbs are attached to the fixed wall with a neighboring limb spacing of $w = 2.25$ cm.

Crustaceans vary in size and their swimmerets can stroke with different frequencies. The Reynolds number is defined as $Re = \hat{L}\hat{U}/\nu$, where \hat{L} is a characteristic length, \hat{U} is a characteristic velocity, and $\nu = 0.01$ cm²/s is the kinematic viscosity of water at 20 °C. We take the limb length l_{limb} as \hat{L} , and the maximal velocity of the limb $u_{max} = (2\pi A l_{limb})/T$ as \hat{U} , where A is the swimmeret stroke amplitude. For example, typical parameters associated with fast forward swimming of Antarctic krill (1) are $l_{limb} \approx 0.5$ cm, $T \approx 0.2$ s, and $A \approx \pi/4$, which give $Re \approx 600$. For adult crayfish (2), $l_{limb} \approx 1$ cm, T ranges from 0.25 to 1 s and $A \approx \pi/8$, which give Reynolds number spanning from 250 to 1,000. Younger crayfish have shorter limbs, which results in Reynolds numbers in the order of 10. In our simulations, we use $Re = 50, 200$, and 800 achieved by fixing $l_{limb} = 1.5$ cm, $A = \pi/4$, and adjusting T accordingly.

The motion of the limbs drives the motion of the surrounding fluid. The equations that determine the motion of the fluid are Navier–Stokes equations:

$$\rho \left(\frac{\partial \vec{u}}{\partial t} + \vec{u} \cdot \nabla \vec{u} \right) = -\nabla p + \mu \Delta \vec{u} + \vec{f}, \quad [S1]$$

$$\nabla \cdot \vec{u} = 0. \quad [S2]$$

The variable t is time, \vec{u} is the fluid velocity, p is the pressure, \vec{f} is the applied force density, ρ is the fluid density, and μ is the viscosity. We use the immersed boundary method, in which structures (limbs and body) are represented in a moving, Lagrangian coordinate system, whereas fluid variables are represented in a fixed, Eulerian coordinated system (3). The force density \vec{f} is determined implicitly by the boundary condition on the immersed structures.

The immersed structures (limbs and wall) are parameterized by arc length s , and their position is denoted by $\vec{X}(s, t)$. We use capital letters $\vec{U}(s, t), \vec{F}(s, t), \vec{X}(s, t)$ for the velocity, force density, and position defined in the Lagrangian coordinates, and lowercase letters for fluid variables in the Eulerian coordinates. The force density $\vec{f}(\vec{x}, t)$ in Eq. 1 is obtained from the force density $\vec{F}(s, t)$ by:

$$\vec{f}(\vec{x}, t) = S(\vec{F}) = \int_{\text{structure}} \vec{F}(s, t) \delta(\vec{x} - \vec{X}(s, t)) ds, \quad [S3]$$

where $\delta(\vec{x})$ is the Dirac delta function. The operator S “spreads” the force density from the immersed boundary coordinates to force density in the fluid coordinates. The fluid velocity interpolated to the immersed structure is:

$$\vec{U}(s, t) = S^*(\vec{u}) = \int_{\text{fluid}} \vec{u}(\vec{x}, t) \delta(\vec{x} - \vec{X}(s, t)) d\vec{x}. \quad [S4]$$

Note that $\vec{U}(s, t)$ is different from the velocity of the limbs prescribed as $\vec{U}_{IB}(s, t) = (\partial \vec{X}(s, t))/\partial t$.

Because the limbs during PS and the body are impermeable, the fluid is forced to move with the prescribed velocity on these structures. When the limbs become permeable during RS, the fluid will permeate through the orthogonal direction \vec{n} of the limb with velocity U_{slip} . Then the velocity of the structures and the fluid satisfy:

$$\vec{U}_{IB}(s, t) = S^*(\vec{u}) - U_{slip} \vec{n}. \quad [S5]$$

The slip velocity is proportional to the pressure jump across the permeable structure, given by $U_{slip} = -\xi[p]$, where ξ is a permeability coefficient. The pressure jump, $[p]$, is related to the immersed boundary force at the limb by $[p] = \vec{F} \cdot \vec{n}$ (4, 5). Therefore, the fluid velocity is required to satisfy:

$$\vec{U}_{IB} = S^*(\vec{u}) + B\vec{F}, \quad [S6]$$

where

$$B = \begin{cases} 0, & \text{on the limbs during PS and on the body,} \\ \xi \vec{n} \vec{n}^T, & \text{on the limbs during RS,} \end{cases} \quad [S7]$$

and \vec{n} is a unit column vector that points at the orthogonal direction of the limb with the positive direction defined as the tail direction. The fluid velocity \vec{u} , pressure p , and the structure force density \vec{F} are determined by the system Eqs. S1, S2, and S6, where the Lagrangian and Eulerian variables are related through Eqs. S3 and S4.

Section 1.2. Biomechanics of Swimmerets and Justification of the Fluid Model Assumptions.

Swimmerets are constructed of a series of three rigid, hollow tubes connected by joints. The tube closest to the body wall, the very short “coxa,” is connected to the body by a joint made of a short section of thinner, flexible membrane that permits large rotation of the joint in one plane. The distal end of coxa is connected by a similar joint to the much longer “basipodite,” which at its distal end is connected again to two “rami” that are the distal ends of the swimmerets. Because the greatest range of rotation is at the base of the limb, at the body wall–coxa joint and the coxa–basipodite joint, we model the swimmeret as a rigid paddle that rotates about its connection to the rigid body. The pair of distal rami are extended during each PS movement, but flexed somewhat during each RS movement, reducing their drag. To approximate this fact that swimmerets are straight and fanned-out during PS and are curled and folded during RS, we treat swimmerets as impermeable during PS and permeable during RS.

The motion of the swimmerets is driven by striated skeletal muscles that change the angle of rotation about the joints. There are two functional sets of muscles, PS muscles and RS muscles, that operate across each joint. The largest muscles operate across the joint that connects the swimmeret to the body (6, 7), and these produce most of the force that drives each PS and RS. This musculature is innervated by motor axons that project from the central pattern generator (CPG) in the abdominal segment on which the swimmeret is mounted. Bursts of action potentials in motor axons lead to bursts of electrical activity in the PS and RS muscles.

Fig. S2 (from ref. 1) shows the position of a swimmeret (i.e., the angle of the joint that connects the swimmeret to the body) and the corresponding electrical activity in power stroke muscles (PSm) and return stroke muscles (RSm). The swimmeret position changes smoothly over time in an almost sinusoidal manner. Note, however, that there are variations from cycle to cycle. Nevertheless, the timing of the swimmeret movements is strongly correlated with the timing of the bursts of muscle activity caused by the motor neuron input. We note further that the distinct tail-to-head metachronal interlimb coordination is maintained in a variety of swimming modes [forward swimming, upside-down swimming, hovering, and tethered swimming (1, 8)] in which the swimmerets experience different hydrodynamic forces. These observations imply that the nonlinearity of muscles and the passive viscoelasticity of the skeleton that complicate analysis of fish swimming (9, 10) are not primary factors for understanding the mechanisms underlying the intersegmental phase differences between swimmerets during swimming in long-tailed crustaceans. Thus, the motion of the swimmerets in a fluid dynamics model can be well approximated by prescribing their positions, as we do in our model.

Section 1.3. Numerical Method for the Fluid Model. The computational domain is a 60-cm-wide and 10-cm-high rectangle for all simulations. We use periodic boundary conditions on all four edges of the rectangular domain to facilitate the use of a Fourier pseudospectral method (11, 12). The fixed horizontal wall that mimics the body is a 60-cm-wide horizontal rigid wall in parallel to the length direction of the domain. This wall enforces the no-slip condition, i.e., the fluid cannot move relative to the wall. Hence, the periodic condition in the vertical direction and the fixed horizontal wall is equivalent to a 10-cm-high channel with no-slip conditions on the top and the bottom of the domain. In all relevant figures, the horizontal wall is visualized a distance of 2 cm from top of the computational domain. Note, however, this 2-cm offset is arbitrary and does not affect the results. The limbs occupy a small rectangular region that is less than 10 cm in width and 4 cm in height (Fig. S3). We use a 60-cm-long domain, which is sufficiently long to allow the velocity field to equilibrate and establish a flow independent of the x coordinate (Fig. S4).

The fluid velocity and pressure are located on a fixed, uniform Eulerian grid with spacing $h = 10/256$ cm; $\vec{x}_{i,j} = (x_i, y_j)$ is the location of the (i, j) th Eulerian fluid grid point. The differential operators in Eqs. S1 and S2 are discretized using the pseudospectral method (11, 12). The immersed structures (the limbs and the wall) are discretized on a moving Lagrangian grid with uniform mesh spacing $\Delta s = h$; $\vec{X}_k = (X_k, Y_k)$ is the location of the k th immersed boundary point. The Dirac delta function in Eqs. S3 and S4 is approximated by $\delta(\vec{x}) \approx \delta_h(x)\delta_h(y)$, where $\vec{x} = (x, y)$ and

$$\delta_h(x) = \begin{cases} \frac{1}{4h} \left(1 + \cos\left(\frac{\pi x}{2h}\right) \right), & \text{if } |x| < 2h, \\ 0, & \text{otherwise.} \end{cases} \quad [\text{S8}]$$

Then the discretized spreading operator S_h and the discretized interpolation operator S_h^* are, respectively,

$$\vec{f}_{i,j} = S_h(\vec{F}) = \Delta s \sum_k \vec{F}_k \delta_h(x_i - X_k) \delta_h(y_j - Y_k), \quad [\text{S9}]$$

$$\vec{U} = S_h^*(\vec{u}) = h^2 \sum_{ij} \vec{u}_{ij} \delta_h(x_i - X_k) \delta_h(y_j - Y_k). \quad [\text{S10}]$$

For temporal discretization, we use the semiimplicit backward differentiation formula method, a second-order implicit-explicit time difference scheme (13) with time step $\Delta t = 2 \times 10^{-4}T$, where

T is the period of the stroke. We use a superscript to denote the time level, e.g., $\vec{u}^n(\vec{x}) = \vec{u}(\vec{x}, n\Delta t)$. The fully discretized system is:

$$\rho \frac{3\vec{u}^{n+1} - 4\vec{u}^n + \vec{u}^{n-1}}{2\Delta t} = -\rho \left(2\vec{u}^n \cdot \nabla_h \vec{u}^n - \vec{u}^{n-1} \cdot \nabla_h \vec{u}^{n-1} \right) - \nabla_h p^{n+1} + \mu \Delta_h \vec{u}^{n+1} + S_h(\vec{F}^{n+1}), \quad [\text{S11}]$$

$$\nabla_h \cdot \vec{u}^{n+1} = 0, \quad [\text{S12}]$$

$$\vec{U}_{\text{IB}}^{n+1} = S_h^*(\vec{u}^{n+1}) + B\vec{F}^{n+1}, \quad [\text{S13}]$$

where ∇_h , $\nabla_h \cdot$, and Δ_h are the discretized spatial differential operators.

Beginning with \vec{u}^{n-1} , \vec{u}^n , \vec{F}^n and given $\vec{U}_{\text{IB}}^{n+1}$, we approximately solve the system (Eqs. S11–S13) to obtain \vec{u}^{n+1} , p^{n+1} , \vec{F}^{n+1} , using the following predictor–corrector method: We first predict the fluid velocity and pressure by advancing Eqs. S11 and S12 using the force density from the previous time step as the initial guess. Then the boundary condition Eq. S13 is enforced to predict the force density. We repeat this process using the predicted force density as the approximation to \vec{F}^{n+1} . Our method is similar to the projection approach of Taira and Colonius (14) and the fractional time stepping of Su, Lai, and Lin (15).

Specifically, our algorithm advances the variables from $t^n = n\Delta t$ to t^{n+1} as follows:

1. Solve Eqs. S11 and S12 for $\vec{u}^{n+1,*}$ using \vec{F}^n as the initial guess for \vec{F}^{n+1} .
2. Perform a projection (15) of $\vec{u}^{n+1,*}$ to enforce the boundary condition (Eq. S13) by solving:

$$\frac{\vec{u}^{n+1} - \vec{u}^{n+1,*}}{\Delta t} = S_h(\delta\vec{F}), \quad [\text{S14}]$$

$$\vec{U}^{n+1} = S_h^*(\vec{u}^{n+1}) + B(\vec{F}^n + \delta\vec{F}), \quad [\text{S15}]$$

for $\delta\vec{F}$.

3. Solve Eqs. S11 and S12 for \vec{u}^{n+1} using $\vec{F}^n + \delta\vec{F}$ as the corrected approximation to \vec{F}^{n+1} .
4. Repeat step 2 to update \vec{F}^{n+1} .

Given the flow field and structure force density, we compute the flux of the fluid by $Q^n = h \sum_j \vec{u}^n(x_{\text{end}}, y_j)$ and the power consumption of the limb movement by $PC^n = \Delta s \sum_k \vec{F}_k^n \cdot \vec{U}_k^n$. Average flux $\langle Q \rangle$ and average power consumption $\langle PC \rangle$ are obtained by taking the time average of Q^n and PC^n over the 10th period, which allows the initial transient flows to dissipate. Then our efficiency measure of the stroke pattern is given by $\langle Q \rangle / \langle PC \rangle$.

Finally, we calculate the average flux produced by consecutive PS and RS of a single limb using different values of nondimensional permeability coefficient $\hat{\xi}$ and Re (Fig. S5). Average flux in general grows positively as $\hat{\xi}$ increases, but its growth rate decreases as $\hat{\xi}$ gets larger. The results shown in the main text are produced using $\hat{\xi} = 0.5$, which produces an intermediate average flux. It is important to note that, although different values of $\hat{\xi}$ lead to different absolute values of average flux, $\hat{\xi}$ does not affect the significant relative advantage of the tail-to-head metachronal wave compared to other metachronies.

In *Discussion* in the main text, we argued that the significant fluid mechanical advantage of the tail-to-head metachronal rhythm of limb movement arises from a robust geometric mechanism based on the asymmetric arrangement of the neighboring limbs during PS and RS. This further implies that, if neighboring limbs are more

closely spaced, the relative advantage of the tail-to-head metachrony (and the relative disadvantage of the hypothetical head-to-tail metachrony) compared to the in-phase rhythm will be augmented. Fig. S6 shows that for tail-to-head metachronies, the average flux indeed increases as the limb spacing w shortens, and for head-to-tail metachronies, the average flux indeed decreases as w shortens. Note that, with a smaller w , neighboring limbs can collide if the phase difference is close to 0.5 (antiphase). To avoid limb collision, the simulations are performed for phase differences that do not lead to collision.

Section 2. Neural Circuit of Swimmeret System

Section 2.1. Neural Circuit of Swimmeret System and Reduction to Phase Model. This subsection provides a detailed description of the neural circuit of the crayfish swimmeret system and explains how it relates to the idealized circuit model and the phase model presented in the main text.

The coordinated movements of swimmerets are driven by a motor pattern generated by neural mechanisms intrinsic to the central nervous system (CNS). The crustacean CNS consists of segmental ganglia connected by axons to form a ventral nerve cord running the length of the body. In those abdominal segments that carry a pair of swimmerets, the segmental ganglion contains two neural modules, each of which contains the complete innervation of one swimmeret. Each swimmeret has its own set of motor neurons that innervate functionally antagonist PS and RS muscles (16).

Our phase models of this nervous system are based on detailed experimental and anatomical descriptions of the cellular components and organization of individual swimmeret modules (16, 17) and similarly detailed descriptions of the components and organization of the intersegmental coordinating circuit (18, 19). In each swimmeret module, a pattern-generating circuit organizes the swimmeret's motor neurons so that PS and RS motor neurons fire alternating bursts of action potentials. Each module can operate independently, but the series of four pairs of modules are normally coordinated by intersegmental connections that impose the phase differences characteristic of swimmeret movements during forward swimming. This distinct pattern can be expressed by the isolated abdominal nerve cord without any need for cycle-by-cycle proprioceptive information (2, 20). These *in vitro* motor patterns, "fictive locomotion," show the same PS–RS alternation and the posterior-to-anterior intersegmental phase delays characteristic of coordinated swimmeret beating (Fig. 3A). These phase relations are maintained through a 10-fold range of periods.

Fig. S7 depicts the synaptic organization of the circuit that generates and coordinates activity in the swimmeret modules in ganglia A2, A3, A4, and A5 (Fig. 3). The key features of the circuit are as follows.

The local circuit in each module produces rhythmic antiphase PS-RS activity. The pattern-generating kernel of each module is formed by non-spiking local interneurons, IPS and IRS, which are connected by reciprocal inhibition. This "half-center" structure produces antiphase activity in the IPS and IRS interneurons that gate their synapses in an on and off manner with an approximately half-period duty cycle. Experimental measurements show that the intrinsic frequencies of the pattern-generating kernels in each module are similar (2). **Ascending output is in-phase with the PS of the local module, whereas descending output is in-phase with the RS of the local module.** The pattern-generating kernel drives the activity of the PS and RS motor neurons and spiking neurons, ASC_E and DSC. ASC_E neurons fire bursts of spikes that are in-phase with the module's PS motor neurons, carrying information of the local module's phase to more anterior modules. DSC neurons fire bursts of spikes that are in phase with the module's RS motor neurons, carrying information of the local module's phase to more posterior modules. **All coordinating input coming into a local module is transmitted to the IRS neuron (through ComInt1).** The local nonspiking interneuron ComInt1 (CI1) is the target of all intersegmental synaptic input to

the module via ASC_E and DSC axons. Each ComInt1 transmits the coordinating information to the IRS neuron in its own pattern-generating kernel. Although each module receives input from all other modules, synaptic connections between nearest-neighbor modules are significantly stronger than longer-range connections (19). Synaptic input from ascending and descending input from neighboring modules onto CI1 are similar in strength and dynamics, and therefore the local oscillating module responds to ascending and descending input in a similar manner.

The idealized model circuit that we describe in the main text highlights the topological structure of the swimmeret circuit. We describe the circuit as a chain of half-centered oscillators (HCOs) that captures all of the key experimentally determined features of the circuit (18, 19, 21). Specifically, (i) each pattern-generating circuit is condensed into a half-center oscillator composed of two reciprocally inhibitory cells, and (ii) the trisynaptic intersegmental connections are collapsed to single monosynaptic connections between cells in the pattern-generating kernels, i.e., ascending connections project from a cell in-phase with the IRS neuron (the R cell) in the more posterior kernel to a cell in-phase with the IRS neuron (the R cell) in the more anterior kernel, whereas descending connections project from a cell in-phase with the IPS neuron (the P cell) in the more anterior kernel to a cell in-phase with the IRS neuron (the R cell) in the more posterior kernel (as shown in Fig. S6 and Fig. 3). This model encapsulates the known cellular composition and synaptic organization of a module's 90–100 neurons. Because longer-range connections are significantly weaker than nearest-neighbor connections, we have not included them in our model.

The main text explains how this idealized model of the circuit is reduced to our phase model. However, it is important to note that we use the idealized model only to simplify the description of the circuit and to highlight the topological structure of the swimmeret circuit. The phase model is in fact more general than the idealized description of the circuit. The basic assumption in all reductions to phase models is that the coupling between oscillators is sufficiently weak, i.e., the dynamics of the oscillators are dominated by internal dynamics and coupling does not alter the activity significantly other than to cause relatively small phase shifts on any particular cycle. This appears to be a reasonable assumption for the swimmeret circuit because perturbations to CI1 that are similar to ASC_E and DSC input result in phase shifts below 10% [phase response curve (PRC) data, Fig. 3C]. Other than this basic assumption, our phase model only assumes that (i) the individual modules are intrinsically oscillating, (ii) ascending output of a module is in antiphase with the descending output, and (iii) ascending and descending inputs have the same effect on a module's phase. These follow directly from the description of the full swimmeret neural circuit described above. It implies that the ascending and descending interaction functions have the same shape. Thus, our phase model captures all of the essential features of the swimmeret circuit and is independent of other details of the system.

Section 2.2. Measuring the Interaction Function of a Local Swimmeret CPG. *The relationship between the interaction function and the PRC of a neural oscillator.* When a stimulus is delivered to a neural oscillator, there is a change in timing of the oscillator, i.e., the stimulus causes a phase shift to occur. The magnitude and the sign of the phase shift depend on the characteristics of the stimulus and the oscillator's phase at the time which the stimulus is delivered. The relationship between the phase shift ($\Delta\theta$) and the phase at which the stimulus is delivered ($\theta = \omega t + \varphi$) is quantified by the PRC of a neural oscillator. When the PRC is generated using a small abrupt (delta function) stimulus and the phase shifts are normalized by the magnitude of the stimulus (i.e., the total charge delivered), it is referred to as the infinitesimal PRC (iPRC) or phase-dependent sensitivity function.

The iPRC $Z(\omega t + \varphi)$ can be viewed as a Green's function or impulse–response function for the neural oscillator and therefore can be used to estimate the oscillator's PRC for arbitrary time-dependent small-magnitude stimuli $I_{\text{stim}}(t)$ (22):

$$\Delta\theta(\varphi) = \int_{t=0}^{\infty} Z(\omega t + \varphi) I_{\text{stim}}(t) dt. \quad [\text{S16}]$$

Note that, if the duration of the stimulus is less than the period of the oscillation T , then

$$\Delta\theta(\varphi) = \int_{t=0}^T Z(\omega t + \varphi) I_{\text{stim}}(t) dt = T \int_{s=0}^1 Z(s + \varphi) I_{\text{stim}}(sT) ds. \quad [\text{S17}]$$

The theory of weakly coupled oscillators uses the iPRC in a similar manner to determine the interaction function between coupled oscillators (23). Specifically, the interaction function H is given by the convolution of the iPRC $Z(\omega t + \varphi_i)$ of the postsynaptic oscillator (i) and the periodic synaptic coupling current $I_{\text{coup}}(t + \varphi_j T)$ that the postsynaptic oscillator receives due to activity in the presynaptic oscillator (j):

$$\begin{aligned} H(-(\varphi_i - \varphi_j)) &= \frac{1}{T} \int_{t=0}^T Z(\omega t + \varphi_i) I_{\text{coup}}((\omega t + \varphi_j)T) dt \\ &= \int_{s=0}^1 Z(s + (\varphi_i - \varphi_j)) I_{\text{coup}}(sT) ds. \end{aligned} \quad [\text{S18}]$$

The above expression for the PRC $\Delta\theta(\varphi)$ and the interaction function $H(-\varphi)$ imply that, if the coupling current $I_{\text{coup}}(t)$ is “on” for less than the full period and the stimulus $I_{\text{stim}}(t)$ is approximately equal to the coupling current $I_{\text{coup}}(t)$, then the interaction function H can be estimated by the PRC as follows:

$$H(-\varphi) = \frac{\Delta\varphi(\varphi)}{T}. \quad [\text{S19}]$$

Measuring the PRC of a local swimmeret CPG. All coordinating information reaches the kernel of each swimmeret CPG through its ComInt1 (CI1) (18, 24). During each cycle of the normal motor pattern in the swimmeret circuit, each coordinating neuron that provides input to a local CPG evokes a burst of synaptic current in CI1 with a duration of approximately one-half of the period, i.e., less than a full period (19). Therefore, an estimate of the interaction function for the local CPGs can be obtained by measuring the PRC of a local CPG using a stimulus that approximates the synaptic current in CI1 evoked by a coordinating neuron during a single cycle.

The PRC of a local swimmeret CPG was measured experimentally by calculating the change in cycle period caused by occasional perturbations of the membrane potential of CI1. In these experiments, the abdominal nerve cord of a crayfish, *Parastacus leniusculus*, was removed to a saline-filled experimental dish, using methods described in detail in ref. 18. Extracellular recording electrodes were placed on PS branches of the nerve innervating selected swimmerets (Fig. 3A) and attached to high-gain preamplifiers. Intracellular recordings from ComInt1 neurons were made with a glass microelectrode attached to an SEC 05 amplifier (npi electronic). These recordings were digitized at 10 kHz with an Axon Instruments Digidata 1322A and analyzed using pClamp (Molecular Devices) and Dataview (www.st-andrews.ac.uk/~wjh/).

In experiments during which the CPG was steadily producing its normal periodic PS bursts, the ComInt1 neuron's membrane potential was voltage clamped using single-electrode voltage-clamp techniques (19). Perturbations of the CPG were caused by step changes from -50 to -25 mV that lasted 250 ms (approximately one-half of the period). Perturbations were delivered at different phases in the CPG's cycle of activity. The period of a cycle, T , was defined as the time from the start of one burst of impulses in the PS recording (Fig. 3A) to the start of the next burst. The phase of the perturbation in the cycle during which it occurred was calculated as the time from the start of the cycle to the start of the step, divided by $\langle T \rangle$ (19). Changes in period were calculated as the difference between the mean period of the four preceding unperturbed cycles, $\langle T \rangle$, and the measured period, T_i , of the cycle in which the step occurred. Normalizing this difference to the mean period, $(\langle T \rangle - T_i)/\langle T \rangle$, and plotting it vs. the phase of the step created the interaction function (Fig. 3C).

In Fig. 3C, a “locally-weighted estimate” curve has been fitted to the experimental data using MATLAB's “robust lowess” function (MathWorks). This function takes into account that the experimental phases were irregularly spaced. To avoid errors in the calculation of these curves near their ends, we took advantage of the periodic property of the motor pattern (Fig. 3A) by extending the data range from 1.0 to 1.25 by copying the points from 0.0 to 0.25, and from -0.75 to 0.0 with points from 0.75 to 1.0. Then we fitted over the range -0.75 to 1.25 and plotted the fitted curve between 0 and 1.0.

Section 2.3. Other Hypothetical Network Topologies in a Chain of HCOs and the Stability of the Phase-Locked Metachronal Patterns.

The key organizational feature of the neural circuit of the crayfish swimmeret system giving rise to the 0.25 phase constancy is the half-center structure of the local CPG and the topology of the intersegmental coupling. To highlight this fact, we determine the invariant phase-locked states that can arise in hypothetical networks with similar circuit properties to the natural crayfish swimmeret circuit. Specifically, we rearrange the intersegmental coupling while preserving the basic circuit properties, i.e., (i) each HCO has one ascending and one descending connection with the same sign (excitatory or inhibitory) and strength, and (ii) the incoming connections target a single cell in the HCO. Under these conditions, there are 32 different network topologies possible between each pair of neighboring HCOs. If we do not immediately distinguish the difference between inhibitory and excitatory connections, there are 16 possible topologies. Using the symmetry that the P and R cells in each HCO are identical and are always in antiphase, we can further reduce the 16 possible topologies to four fundamentally different network topologies shown in Fig. 3D.

The network topologies (s1) and (s2) are symmetric in the sense that both the ascending and descending connections are between either two P cells or one P cell and one R cell, whereas the network topologies (a1) and (a2) are asymmetric because one of the two connections goes from P to P (or R to R) and the other connection goes from P to R (or R to P). The asymmetric topology (a1) corresponds to the natural crayfish swimmeret system. Note that longer-range connections exist (e.g., between the most anterior HCO and the most posterior HCO). However, the nearest-neighbor coupling are significantly stronger than longer-range coupling (19), and therefore longer-range connections are not included in our model.

A pair of HCOs: Existence and stability of phase constant rhythms. We have shown in the main text that phase differences $\Delta\theta = 0.25$ and 0.75 are two phase-locked states under crayfish's asymmetric network topology (a1) regardless of the specific shape of the interaction function H . Here, we examine the existence and stability of phase-locked states in the other three network topologies, (a2), (s1), and (s2) (Fig. 3D).

Recall that, in main text, we defined $H(\Delta\theta)$ to be the interaction function for an ascending input from an R cell to an R cell, and consequently, $H(-\Delta\theta+0.5)$ to be the interaction function for a descending input from P to R. With the above convention, we have the following:

- Under the asymmetric topology (a2), because the ascending input is from R to P, this input is effectively phase delayed by a half-period with respect to an ascending input from R to R. Thus, the interaction function for the ascending connection in this (a2) topology is $H(\Delta\theta+0.5)$. Because the descending input is from P to P, this input is effectively phase delayed by a half-period with respect to a descending input from P to R. Thus, the interaction function for the descending connection in this (a2) topology is $H((-\Delta\theta+0.5)+0.5)=H(-\Delta\theta)$.
- Under the symmetric topology (s1), because both the ascending and descending connections are between P cells, the ascending input is effectively in-phase with an ascending input from R to R, and the descending input is effectively phase delayed by a half-period with respect to a descending input from P to R. Thus, the interaction functions for the ascending and descending connections are $H(\Delta\theta)$ and $H((-\Delta\theta+0.5)+0.5)=H(-\Delta\theta)$, respectively.
- Under the symmetric topology (s2), because both the descending and ascending connections are from an R cell to a P cell, the ascending input is effectively phase delayed by a half-period with respect to an ascending input from R to R, and the descending input is effectively in-phase with a descending input from P to R. Thus, the interaction functions for the ascending and descending connections are $H(\Delta\theta+0.5)$ and $H(-\Delta\theta+0.5)$, respectively.

Using a general notation, the dynamics of the phase difference between a pair of HCOs are described by the phase model:

$$\frac{d\Delta\theta}{dt} = H(-\Delta\theta + \varphi_1) - H(\Delta\theta + \varphi_2) =: G(\Delta\theta), \quad [\text{S20}]$$

where $\varphi_1 = 0.5, \varphi_2 = 0$ for (a1) topology, $\varphi_1 = 0, \varphi_2 = 0.5$ for (a2) topology, $\varphi_1 = \varphi_2 = 0$ for (s1) topology, and $\varphi_1 = \varphi_2 = 0.5$ for (s2) topology. A phase-locked state of the coupled oscillators with $\Delta\theta^*$ phase difference (i.e., a steady state of the dynamical system described by Eq. S20) corresponds to $G(\Delta\theta^*) = 0$. Noting that H has a period of 1, it can readily be seen that $\Delta\theta^* = 0$ and 0.5 are two invariant phase-locked states under the two symmetric network topologies (s1) and (s2). Similarly, $\Delta\theta^* = 0.25$ and 0.75 are two invariant phase-locked states under the two asymmetric network topologies (a1) and (a2).

The stability of these phase-locked states with $\Delta\theta^*$ phase difference depends on the sign of $G'(\Delta\theta^*) = -H'(-\Delta\theta + \varphi_1) - H'(\Delta\theta + \varphi_2)$.

A chain of four HCO: Existence and stability of phase constant rhythms.

We extend the analysis of the two-HCO model above to a four-HCO model with nearest-neighbor coupling. The phase differences in a four-HCO chain are $(\Delta\theta_1, \Delta\theta_2, \Delta\theta_3) = (\theta_2 - \theta_1, \theta_3 - \theta_2, \theta_4 - \theta_3)$. A phase-locked state $(\Delta\theta^*, \Delta\theta^*, \Delta\theta^*)$ that corresponds to a meta-chronal wave in a four-HCO chain satisfies the following:

$$\begin{aligned} H(\Delta\theta^* + \varphi_2) + H(-\Delta\theta^* + \varphi_1) - H(\Delta\theta^* + \varphi_2) &= 0, \\ H(\Delta\theta^* + \varphi_2) + H(-\Delta\theta^* + \varphi_1) - H(\Delta\theta^* + \varphi_2) - H(-\Delta\theta^* + \varphi_1) &= 0, \\ H(-\Delta\theta^* + \varphi_1) - H(\Delta\theta^* + \varphi_2) - H(-\Delta\theta^* + \varphi_1) &= 0, \end{aligned} \quad [\text{S21}]$$

where φ_1, φ_2 are the phase shifts determined by the neural circuit topology (as defined in the previous subsection on the two-HCO system). Using the same analysis for the $(0.25, 0.25, 0.25)$ phase-locked state (referred simply as the 0.25 phase-locked state) in the main text, we obtain the conditions, listed in Table S1, for the existence of other phase-locked states (i.e., in-phase, 0.5 phase locking, and 0.75 phase locking) for each of the four distinct network topologies. With an appropriate network topology as determined by the two-HCO system, the restrictions on H will be reduced to a single condition [$H(\Delta\theta^*) = 0$ or $H(-\Delta\theta^*) = 0$] for the phase-locked state $\Delta\theta^* = 0, 0.25, 0.5$, or 0.75 . This strict condition can be further relaxed by allowing a small deviation from the exact phase-locked state to be $(\Delta\theta_1, \Delta\theta_2, \Delta\theta_3) = (\Delta\theta^* + \varepsilon, \Delta\theta^*, \Delta\theta^* - \varepsilon)$, where ε is a small constant. Specifically, substituting the phase-locked state $(\Delta\theta^* + \varepsilon, \Delta\theta^*, \Delta\theta^* - \varepsilon)$ in Eq. S21 leads to a single algebraic equation of the form $H(\pm\Delta\theta^*) + H(\pm\Delta\theta^* \mp \varepsilon) - H(\pm\Delta\theta^* \pm \varepsilon) = 0$. Because we assume ε is small, this is equivalent to the condition that $(H(\pm\Delta\theta^*)) / (2H'(\pm\Delta\theta^*))$ is small. The exact conditions for the existence of an approximate $\Delta\theta^*$ phase-locked state under the four distinct network topologies are summarized in Table S1.

It is important to note that the topology of the four-HCO chain provides a robust mechanism for generating phase constant rhythm with minimal requirement independently of the biophysical details. Specifically, we do not need multiple conditions on H , and therefore careful tuning of the HCO's properties or the synaptic dynamics is not necessary to achieve the 0.25 or 0.75 phase constancy with an asymmetric network topology, or to achieve a 0 or 0.5 phase constancy with a symmetric topology. However, it would require more than one condition for an asymmetric topology to have phase constancies other than 0.25 or 0.75, or for a symmetric topology to have phase constancies other than the in-phase or anti-phase rhythm.

The stability of the phase-locked state $(\Delta\theta_1, \Delta\theta_2, \Delta\theta_3) = (\Delta\theta^* + \varepsilon, \Delta\theta^*, \Delta\theta^* - \varepsilon)$ depends on the eigenvalues of the Jacobian matrix of the left-hand side of Eq. S21:

$$J(\Delta\theta^*, \varepsilon) = \begin{pmatrix} -H'(-\Delta\theta^* - \varepsilon + \varphi_1) - H'(\Delta\theta^* + \varepsilon + \varphi_2) & H'(\Delta\theta^* + \varphi_2) & 0 \\ H'(-\Delta\theta^* - \varepsilon + \varphi_1) & -H'(-\Delta\theta^* + \varphi_1) - H'(\Delta\theta^* + \varphi_2) & H'(\Delta\theta^* - \varepsilon + \varphi_2) \\ 0 & H'(-\Delta\theta^* + \varphi_1) & -H'(-\Delta\theta^* + \varepsilon + \varphi_1) - H'(\Delta\theta^* - \varepsilon + \varphi_2) \end{pmatrix}.$$

The phase-locked state $\Delta\theta^*$ is stable if $G'(\Delta\theta^*) < 0$, unstable if $G'(\Delta\theta^*) > 0$. For example, a stable phase-locked state at $\Delta\theta^* = 0.25$ arising in the natural asymmetric topology (a1) of the crayfish swimmeret system requires that $H'(0.25) > 0$. On the other hand, the stable phase-locked state at $\Delta\theta^* = 0.25$ arising in the hypothetical asymmetric topology (a2) requires that $H'(0.75) > 0$.

The phase-locked state $(\Delta\theta^* + \varepsilon, \Delta\theta^*, \Delta\theta^* - \varepsilon)$ is stable if matrix J is negative-definite and is unstable otherwise. With sufficiently small ε , the eigenvalues of J are approximately equal to the eigenvalues of $J(\Delta\theta^*, 0)$. With an appropriate network topology for the phase-locked state $\Delta\theta^* = 0, 0.25, 0.5$, or 0.75 , matrix $J(\Delta\theta^*, 0)$ takes the form:

$$H'(\pm \Delta\theta^*) \begin{pmatrix} -2 & 1 & 0 \\ 1 & -2 & 1 \\ 0 & 1 & -2 \end{pmatrix}.$$

Therefore, the stability of the phase-locked state is determined by the sign of $H'(\pm \Delta\theta^*)$. Notice that this gives the same stability conditions as in the two-HCO case. For example, a stable phase-locked state at $\Delta\theta^* = 0.25$ arising in the natural asymmetric topology (a1) of the crayfish swimmeret system requires that $H'(0.25) > 0$. On the other hand, the stable phase-locked state at $\Delta\theta^* = 0.25$ arising in the hypothetical asymmetric topology (a2) requires that $H'(0.75) > 0$. As presented in the main text, experimentally measured H shows that $H'(0.25) > 0$ but $H'(0.75) < 0$ (Fig. 3C), which are consistent with our model predications. The stability conditions of phase constancies in the four distinct network topologies are summarized in Table S2.

Section 2.4. Equal Ascending and Descending Connection Strengths Minimize the Deviation of the Phase-Locked Metachronal Pattern from 0.25. If the strengths of the ascending and descending connections are allowed to differ, then a deviation of the phase lag from 0.25 is expected. In this subsection, we show that ascending and descending connections with the same strength minimize this deviation.

The dynamics of the phase differences between each neighboring HCO ($\Delta\theta_1, \Delta\theta_2, \Delta\theta_3$) are described by Eq. 4 in main text. Under crayfish's (a1) circuit topology, the descending inputs are effectively phase delayed by a half-period with respect to the ascending inputs, i.e., $H_{\text{asc}}(\theta_2 - \theta_1) = \alpha H(\theta_2 - \theta_1)$ and $H_{\text{dsc}}(\theta_1 - \theta_2) = \beta H(\theta_1 - \theta_2 + 0.5)$, where α, β are the strengths of the ascending and descending connections, respectively. When $\alpha \neq \beta$, we expect a deviation of the phase-locked state from (0.25, 0.25, 0.25). Suppose $(\Delta\theta_1, \Delta\theta_2, \Delta\theta_3) = (0.25 + \varepsilon_1, 0.25 + \varepsilon_2, 0.25 + \varepsilon_3)$ is the phase-locked state, where ε_i describe the deviation. If ε_i are small, and the interaction function H is smooth near 0.25, then $(0.25 + \varepsilon_1, 0.25 + \varepsilon_2, 0.25 + \varepsilon_3)$ is a phase-locked state if and only if the following equations are satisfied:

$$\begin{aligned} (a+1)\varepsilon_1 - a\varepsilon_2 - r &= 0, \\ \varepsilon_1 - (a+1)\varepsilon_2 + a\varepsilon_3 &= 0, \\ \varepsilon_2 - (a+1)\varepsilon_3 - ar &= 0, \end{aligned} \quad [\text{S22}]$$

where $a = \alpha/\beta$ and $r = (H(0.25))/H'(0.25)$. Writing ε_i in terms of a and r , we have the following:

$$\begin{aligned} \varepsilon_1 &= -\frac{a^3 - a^2 - a - 1}{a^3 + a^2 + a + 1}r, \\ \varepsilon_2 &= -\frac{a^2 - 1}{a^2 + 1}r, \\ \varepsilon_3 &= -\frac{a^3 + a^2 + a - 1}{a^3 + a^2 + a + 1}r. \end{aligned} \quad [\text{S23}]$$

When the ascending and descending connections have the same strength, the phase-locked state reduces to the case we have already discussed in the main text, i.e., when $a = 1$, we have $\varepsilon_1 = 0.5r$, $\varepsilon_2 = 0$, $\varepsilon_3 = -0.5r$. In fact, this is the minimal deviation from the (0.25, 0.25, 0.25) phase-locked state under the 2-norm $\sqrt{\sum_{i=1}^3 \varepsilon_i^2}$. It can be shown that $\sum_{i=1}^3 \varepsilon_i^2$ reaches its unique global minimum $(1/2)r^2 = (1/2)(H(0.25)/H'(0.25))^2$ when $a = (\alpha/\beta) = 1$. Hence, equal strengths of ascending and descending connections minimize the deviation of the phase-locked metachronal stroke pattern from 0.25.

Section 2.5. Robust Phase Constancy for HCOs with Multiple Ascending and Descending Connections. If connections between each component of neighboring HCOs are permitted, then circuit topologies other

than (a1) can produce robust phase locking with phase lags of 0.25, but these connectivity schemes would have symmetries analogous to the (a1) connection scheme. That is, descending connections must link P and R cells, whereas ascending connections must link R cells to R cells and/or P cells to P cells, and the connection strengths must be appropriately balanced.

Consider two HCOs with general connectivity. Let α_{XY} be the relative strength of the ascending connection between cell X and Y , and β_{XY} be the relative strength of the descending connection between cell X and Y , where X and Y are either P or R . The phase model that governs the evolution of the phase difference between HCOs is given by:

$$\begin{aligned} \frac{d\Delta\theta}{dt} = G(\Delta\theta) &= \{\beta_{PP}H(-\Delta\theta) + \beta_{RR}H(-\Delta\theta) + \beta_{PR}H(-\Delta\theta + 0.5) \\ &+ \beta_{RP}H(-\Delta\theta + 0.5)\} \\ &- \{\alpha_{PP}H(\Delta\theta) + \alpha_{RR}H(\Delta\theta) + \alpha_{PR}H(\Delta\theta + 0.5) \\ &+ \alpha_{RP}H(\Delta\theta + 0.5)\}. \end{aligned} \quad [\text{S24}]$$

Therefore, the condition for the $\Delta\theta^* = 0.25$ phase-locked state is as follows:

$$\begin{aligned} G(0.25) &= (\beta_{PP} + \beta_{RR} - \alpha_{PR} - \alpha_{RP})H(-0.25) \\ &+ (\beta_{PR} + \beta_{RP} - \alpha_{PP} - \alpha_{RR})H(0.25) = 0, \end{aligned} \quad [\text{S25}]$$

which for general $H(\Delta\theta)$ requires that

$$\alpha_{PP} + \alpha_{RR} = \beta_{PR} + \beta_{RP} \quad [\text{S26}]$$

and

$$\alpha_{PR} + \alpha_{RP} = \beta_{PP} + \beta_{RR}. \quad [\text{S27}]$$

The condition for stability of the $\Delta\theta^* = 0.25$ phase-locked state is as follows:

$$\begin{aligned} G'(0.25) &= -(\beta_{PP} + \beta_{RR} + \alpha_{PR} + \alpha_{RP})H'(-0.25) \\ &- (\beta_{PR} + \beta_{RP} + \alpha_{PP} + \alpha_{RR})H'(0.25) < 0. \end{aligned} \quad [\text{S28}]$$

Assuming that the connectivity is effectively excitatory $\alpha_{XY} > 0$ and $\beta_{XY} > 0$, and that $H'(-0.25) < 0$ and $H'(0.25) > 0$ (as shown in the swimmeret module's PRC in Fig. 3 of the main text), Inequality S28 implies that descending connections between P cell and P cell and between R cell and R cell and ascending connections between R cell and P cell act to destabilize the $\Delta\theta^* = 0.25$ phase-locked state. Thus, to maximize stability and robustness:

$$\beta_{PP} = \beta_{RR} = \alpha_{PR} = \alpha_{RP} = 0. \quad [\text{S29}]$$

This, in turn, implies that all descending connections must link P and R cells, whereas ascending connection must link R cells to R cells and/or P cells to P cells. Furthermore, from condition S26, the net ascending connection strength must equal the net descending connection strength. Any connectivity scheme that fulfills these requirements would provide the same robustness of the $\Delta\theta^* = 0.25$ phase-locked state for a fixed value of total connectivity strength. However, it is likely that circuits with single ascending and descending connections would be preferable for energetic reasons. Therefore, the (a1) connection scheme (or a connection scheme with all R and P cells exchanged) seems to be superior to all other connectivity structures.

Section 2.6. Generic Phase Response Properties of HCOs. It can be shown that the stability condition [$H'(0.25) > 0$] and the existence condition [$\varepsilon = H(0.25)/2H'(0.25)$ is small] for the tail-to-head 0.25 phase locking arise from the generic properties of HCOs. Using perturbation and averaging theory, the interaction function H can be expressed as a convolution of the intersegmental input into the HCO, $I(t)$, and the infinitesimal PRC (iPRC) of the HCO, $Z(\theta)$,

$$H(\theta) = \int_0^1 Z(s) \cdot I(s + \theta) ds \quad [\text{S30}]$$

(ref. 23). iPRCs measure the normalized phase shift of an oscillator in response to a brief perturbation as a function of the timing of the input. Under the additional assumptions that the input $I(t)$ is fully on when the presynaptic cell is active and is fully off when the presynaptic cell is suppressed and $I(t)$ activates and deactivates instantaneously with a duty cycle of a half-period, i.e., $I(t)$ is a square wave oscillating between 0 and 1, it follows that

$$H'(0.25) = Z(-0.25) - Z(-0.25 + 0.5) = Z(0.75) - Z(0.25), \quad [\text{S31}]$$

and

$$\varepsilon \approx \frac{H(0.25)}{2H'(0.25)} = \frac{\int_{0.25}^{0.75} Z(s + 0.5) ds}{2[Z(0.75) - Z(0.25)]}. \quad [\text{S32}]$$

We recently showed that canonical models of HCOs, e.g., the Wang–Rinzel HCO model (25), have stereotypical phase response properties: HCO's iPRC $Z(\theta)$ always has either a dominant-negative region (phase delaying) in the first half of the period or a dominant-positive region (phase advancing) in the second half of the period, or a mixture of both (26). The presence of the phase-advancing region in the second half of the period and/or the presence of the phase-delaying region in the first half of the period suggests that $H'(0.25) = Z(0.75) - Z(0.25) > 0$ and that $\int_{0.25}^{0.75} Z(s + 0.5) ds \ll 2[Z(0.75) - Z(0.25)]$. For example, if the iPRC is sinusoidal such as $Z(\theta) = -\sin(2\pi\theta)$, then we have $H'(0.25) > 0$ and $\varepsilon = 0$. In the extreme case that the iPRC is completely flat in the first half of the period and has a positive bump in the second half of the period, i.e., $Z(\theta) = 0$ for $0 \leq \theta < 0.5$, $Z(\theta) = -\sin(2\pi\theta)$ for $0.5 \leq \theta < 1$, we would have $H'(0.25) > 0$ and $\varepsilon \approx 0.08$. Therefore, both the existence condition and the stability condition for the 0.25 phase constancy are satisfied in a robust manner as a result of the generic phase response properties of HCOs.

Section 3. The Effects of Proprioceptive Reflexes on Swimmeret Coordination

The hydrodynamics forces (i.e., forces due to water movement) generated by the movement of a swimmeret can affect the motion of the other swimmerets directly and indirectly through the activation of proprioceptive reflexes. As argued in *SI Text*, section 1.2, the direct effects of hydrodynamic forces on interlimb coordination appear to be minor relative to the effects of the forces generated by the muscles. Extensive experimental evidence suggests that the indirect coupling between swimmerets via proprioceptive feedback also has little effect on interlimb coordination.

In preparations displaying fictive locomotion, movements imposed on an individual swimmeret do not significantly affect the period of the system's output and have little effect on the phase of the motor drive to the moved swimmeret (27, 28). Holding a swimmeret in the fully retracted position that it reaches at the end of each PS strongly activates its major proprioceptors (27, 29), strengthens RS bursts that resist the retraction, and weakens PS burst that assist it. However, it does not stop the cycles of PS–RS bursts to that swimmeret or alter the duty cycles of the PS and RS motor pools or affect the system's period (30). This maintained extreme retraction does cause slight shifts in the phases of PS bursts in neighboring ganglia (less than or equal to -0.06), but does not affect the strengths of those neighboring bursts (30). These experimental results support the view that the temporal structure of the coordinated swimmeret motor pattern is predominately established by the neural circuits in the animal's CNS and is not strongly dependent on proprioceptive input from the individual swimmerets.

We note that the above observations do not imply that the effect of proprioceptive feedback on the motion of an individual swimmeret is insignificant. The proprioceptive innervation of each swimmeret includes setae that are bent by water movements, joint receptors that monitor changes in joint angles, and stretch receptors that monitor the angle of the swimmeret relative to the abdomen (2, 31). During each PS, water flowing around the swimmeret bends these setae and activates a local reflex that increases firing of PS motor neurons, including a subset of these neurons that innervate curler muscles of the rami (32, 33). As cycle periods decrease, the velocities of PS movements increase and encounter increased resistance. Proprioceptive reflexes appear to be able to increase the PS motor drive to compensate for increasing load on the limb. However, the extent to which this “load compensation” is necessary for maximally effective movements remains unresolved.

- Murphy DW, Webster DR, Kawaguchi S, King R, Yen J (2011) Metachronal swimming in Antarctic krill: Gait kinematics and system design. *Mar Biol* 158(11):2541–2554.
- Mulloney B, Smarandache-Wellmann C (2012) Neurobiology of the crustacean swimmeret system. *Prog Neurobiol* 96(2):242–267.
- Peskin CS (2002) The immersed boundary method. *Acta Numer* 11:479–517.
- Kim Y, Peskin CS (2006) 2-D parachute simulation by the immersed boundary method. *SIAM J Sci Comput* 28(6):2294–2312.
- Stockie JA (2009) Modelling and simulation of porous immersed boundaries. *Comput Struct* 87(11–12):701–709.
- Davis WJ (1968) The neuromuscular basis of lobster swimmeret beating. *J Exp Biol* 168(3):363–378.
- Davis WJ (1969) The neural control of swimmeret beating in the lobster. *J Exp Biol* 50(1):99–117.
- Alben S, Spears K, Garth S, Murphy D, Yen J (2010) Coordination of multiple appendages in drag-based swimming. *J R Soc Interface* 7(52):1545–1557.
- McMillen T, Williams T, Holmes P (2008) Nonlinear muscles, passive viscoelasticity and body taper conspire to create neuromechanical phase lags in anguilliform swimmers. *PLoS Comput Biol* 4(8):e1000157.
- Tytell ED, Hsu C-Y, Williams TL, Cohen AH, Fauci LJ (2010) Interactions between internal forces, body stiffness, and fluid environment in a neuromechanical model of lamprey swimming. *Proc Natl Acad Sci USA* 107(46):19832–19837.
- Peyret R (2002) *Spectral Methods for Incompressible Viscous Flow* (Springer, New York).
- Canuto C, Hussaini M, Quarteroni A, Zang T (1993) *Spectral Method in Fluid Dynamics* (Springer, New York).
- Ascher UM, Ruuth SJ, Wetton BTR (1995) Implicit explicit methods for time-dependent partial-differential equations. *SIAM J Numer Anal* 32(3):797–823.
- Taira K, Colonius T (2007) The immersed boundary method: A projection approach. *J Comput Phys* 225(2):2118–2137.
- Su S-W, Lai M-C, Lin C-A (2007) An immersed boundary technique for simulating complex flows with rigid boundary. *Comput Fluids* 36(2):313–324.
- Mulloney B, Hall WM (2000) Functional organization of crayfish abdominal ganglia. III. Swimmeret motor neurons. *J Comp Neurol* 419(2):233–243.
- Smarandache-Wellmann C, Weller C, Wright TM, Jr, Mulloney B (2013) Five types of nonspiking interneurons in local pattern-generating circuits of the crayfish swimmeret system. *J Neurophysiol* 110(2):344–357.
- Smarandache-Wellmann C, Weller C, Mulloney B (2014) Mechanisms of coordination in distributed neural circuits: Decoding and integration of coordinating information. *J Neurosci* 34(3):793–803.
- Smarandache C, Hall WM, Mulloney B (2009) Coordination of rhythmic motor activity by gradients of synaptic strength in a neural circuit that couples modular neural oscillators. *J Neurosci* 29(29):9351–9360.

20. Hughes GM, Wiersma CAG (1960) The co-ordination of swimmeret movements in the crayfish, *Procambarus clarkii* (Girard). *J Exp Biol* 37(4):657–672.
21. Smarandache-Wellmann C, Grätsch S (2014) Mechanisms of coordination in distributed neural circuits: Encoding coordinating information. *J Neurosci* 34(16):5627–5639.
22. Netoff T, Schwemmer MA, Lewis TJ (2012) Experimentally estimating phase response curves of neurons: Theoretical and practical issues. *Phase Response Curves in Neuroscience: Theory, Experiment, and Analysis*, eds Schultheiss NW, Prinz AA, Butera RJ (Springer, New York), Vol 6, pp 95–129.
23. Schwemmer MA, Lewis TJ (2012) The theory of weakly coupled oscillators. *Phase Response Curves in Neuroscience: Theory, Experiment, and Analysis*, eds Schultheiss NW, Prinz AA, Butera RJ (Springer, New York), Vol 6, pp 3–31.
24. Mulloney B, Hall WM (2003) Local commissural interneurons integrate information from intersegmental coordinating interneurons. *J Comp Neurol* 466(3):366–376.
25. Wang X-J, Rinzal J (1992) Alternating and synchronous rhythms in reciprocally inhibitory model neurons. *Neural Comput* 4(1):84–97.
26. Zhang C, Lewis TJ (2013) Phase response properties of half-center oscillators. *J Comput Neurosci* 35(1):55–74.
27. Heitler WJ (1982) Non-spiking stretch receptors in the crayfish swimmeret system. *J Exp Biol* 96(1):355–366.
28. Deller SRT, MacMillan DL (1989) Entrainment of the swimmeret rhythm of the crayfish to controlled movements of some of the appendages. *J Exp Biol* 144(1):257–278.
29. MacMillan DL, Deller SRT (1989) Sensory systems in the swimmerets of the crayfish *Cherax destructor* and their effectiveness in entraining the swimmeret rhythm. *J Exp Biol* 144(1):279–301.
30. Mulloney B, Smarandache-Wellmann CR, Weller C, Hall WM, DiCaprio RA (2014) Proprioceptive feedback modulates coordinating information in a system of segmentally-distributed microcircuits. arXiv:1407.3249 [q-bio.NC].
31. Cattaert D, Le Ray D (2001) Adaptive motor control in crayfish. *Prog Neurobiol* 63(2):199–240.
32. Cattaert D, Clarac F (1987) Rami motor neurons and motor control of the swimmeret system of *Homarus gammarus*. *J Comp Physiol A* 160(1):55–68.
33. Davis WJ (1969) Reflex organization in the swimmeret system of the lobster. I. Intrasegmental reflexes. *J Exp Biol* 51(1):547–564.

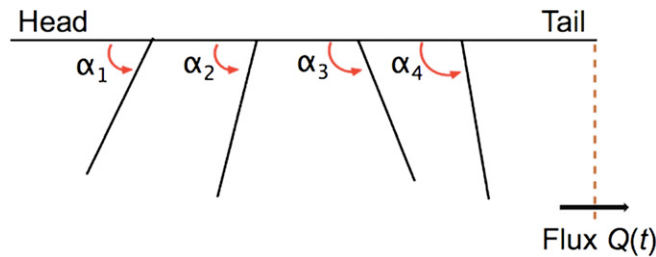


Fig. S1. Fluid model of the swimmeret paddling. The four rigid paddles mimic the limbs (swimmerets) and are attached to a fixed wall that represents the body. These structures are immersed in a two-dimensional fluid. The angle $\alpha_i(t)$ between the limb and the body is a prescribed function of time. The flux $Q(t)$ measures the volume of fluid passing through a vertical line across the domain per unit time.

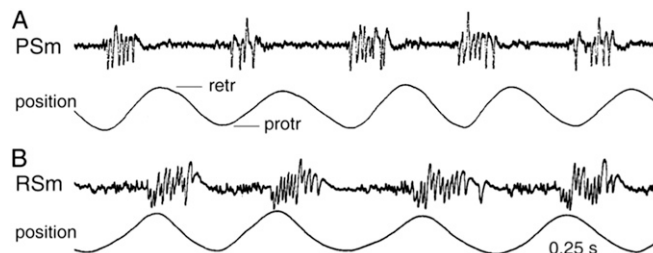


Fig. S2. Simultaneous recordings of swimmeret movements and electrical activity in swimmeret muscles of lobster, *Homarus*. Notice that the periods of these movements are neither constant nor the same, but that relative to these movements the phases of power stroke muscle (PSm) and return stroke muscle (RSm) bursts are stable. (A) Recordings from a PSm and the position of the swimmeret this muscle moved. Bursts of spikes are electrical impulses caused by bursts of presynaptic spikes in the PS motor neurons that innervated this muscle. Position: a continuous record of the swimmeret's periodic movements from its anterior position (protr) to its posterior position (retr). Each upward deflection corresponds to a PS movement. (B) Recordings from a RSm in a separate experiment, and the position of the swimmeret this muscle moved. Bursts of spikes are electrical impulses caused by bursts of spikes in the RS motor neurons that innervated this muscle. Position: same as A. The time scale of the two recordings are the same, but the gains of the two position traces are not known to be the same. (Reprinted with permission from ref. 6.)

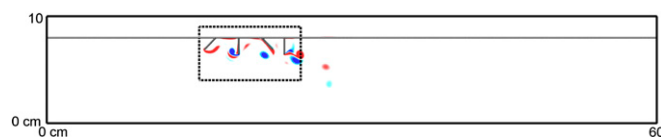


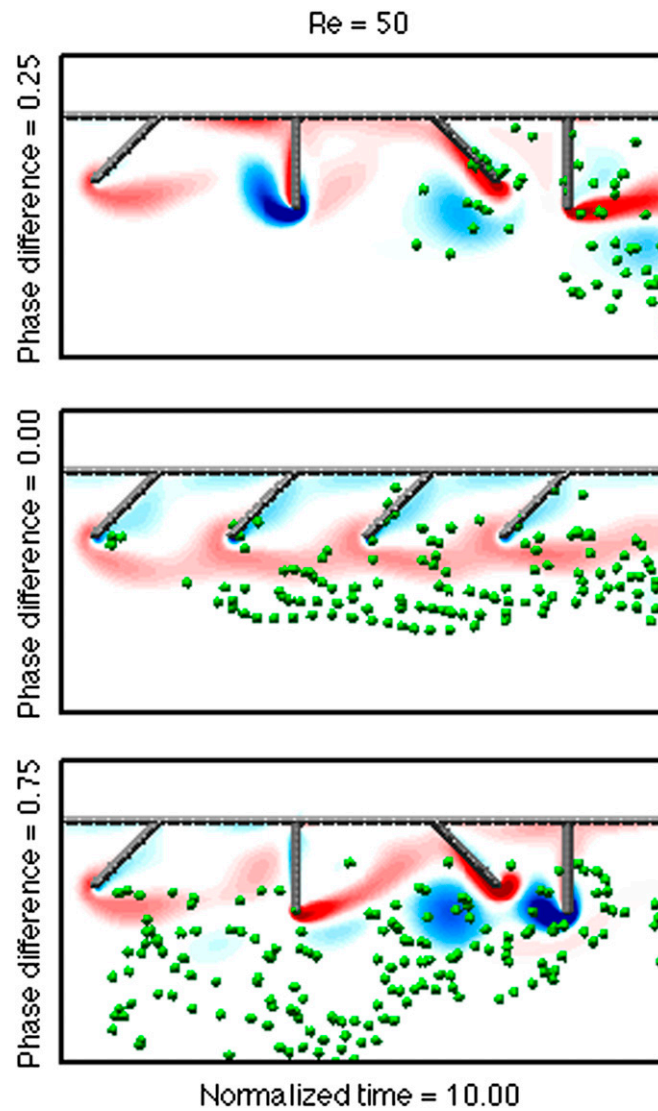
Fig. S3. The entire computational domain. The snapshot of the flow field under the natural tail-to-head metachrony with 0.25 phase difference at $Re = 200$ at the end of the 10th stroke period. The vorticity of the flow field is shown in red–white–blue color (red denotes positive vorticity, and blue denotes negative vorticity). The length of the domain is 60 cm, and the height of the domain is 10 cm. The rectangular region enclosed by dashed boundaries is the region shown in Fig. 2A of the main text and in [Movies S1–S3](#).

Table S1. Conditions for the existence of robust phase constancies in a chain of four HCOs under four distinct network topologies

	Network topology (s1)	Network topology (s2)	Network topology (a1)	Network topology (a2)
0 phase constancy	$H(0) = 0$	$H(0.5) = 0$	Multiple restrictions on H required	Multiple restrictions on H required
0.25 phase constancy	Multiple restrictions on H required	Multiple restrictions on H required	$H(0.25) = 0$	$H(0.75) = 0$
0.5 phase constancy	$H(0.5) = 0$	$H(0) = 0$	Multiple restrictions on H required	Multiple restrictions on H required
0.75 phase constancy	Multiple restrictions on H required	Multiple restrictions on H required	$H(0.75) = 0$	$H(0.25) = 0$
Approximate 0 phase constancy	$\varepsilon \approx \frac{H(0)}{2H'(0)}$ is small	$\varepsilon \approx \frac{H(0.5)}{2H'(0.5)}$ is small	Multiple restrictions on H required	Multiple restrictions on H required
Approximate 0.25 phase constancy	Multiple restrictions on H required	Multiple restrictions on H required	$\varepsilon \approx \frac{H(0.25)}{2H'(0.25)}$ is small	$\varepsilon \approx \frac{H(0.75)}{2H'(0.75)}$ is small
Approximate 0.5 phase constancy	$\varepsilon \approx \frac{H(0.5)}{2H'(0.5)}$ is small	$\varepsilon \approx \frac{H(0)}{2H'(0)}$ is small	Multiple restrictions on H required	Multiple restrictions on H required
Approximate 0.75 phase constancy	Multiple restrictions on H required	Multiple restrictions on H required	$\varepsilon \approx \frac{H(0.75)}{2H'(0.75)}$ is small	$\varepsilon \approx \frac{H(0.25)}{2H'(0.25)}$ is small

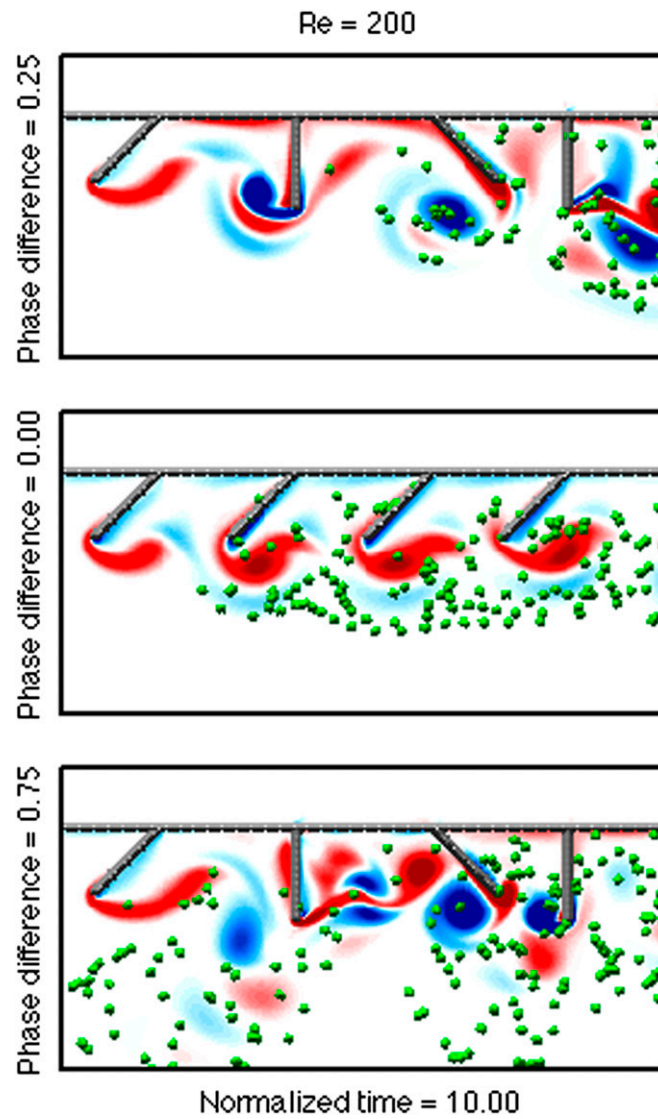
Table S2. Stability conditions for the robust phase constancies in a chain of four HCOs under four distinct network topologies

	Network topology (s1)	Network topology (s2)	Network topology (a1)	Network topology (a2)
0 phase constancy	$H'(0) > 0$	$H'(0.5) > 0$	Multiple restrictions on H required	Multiple restrictions on H required
0.25 phase constancy	Multiple restrictions on H required	Multiple restrictions on H required	$H'(0.25) > 0$	$H'(0.75) > 0$
0.5 phase constancy	$H'(0.5) > 0$	$H'(0) > 0$	Multiple restrictions on H required	Multiple restrictions on H required
0.75 phase constancy	Multiple restrictions on H required	Multiple restrictions on H required	$H'(0.75) > 0$	$H'(0.25) > 0$



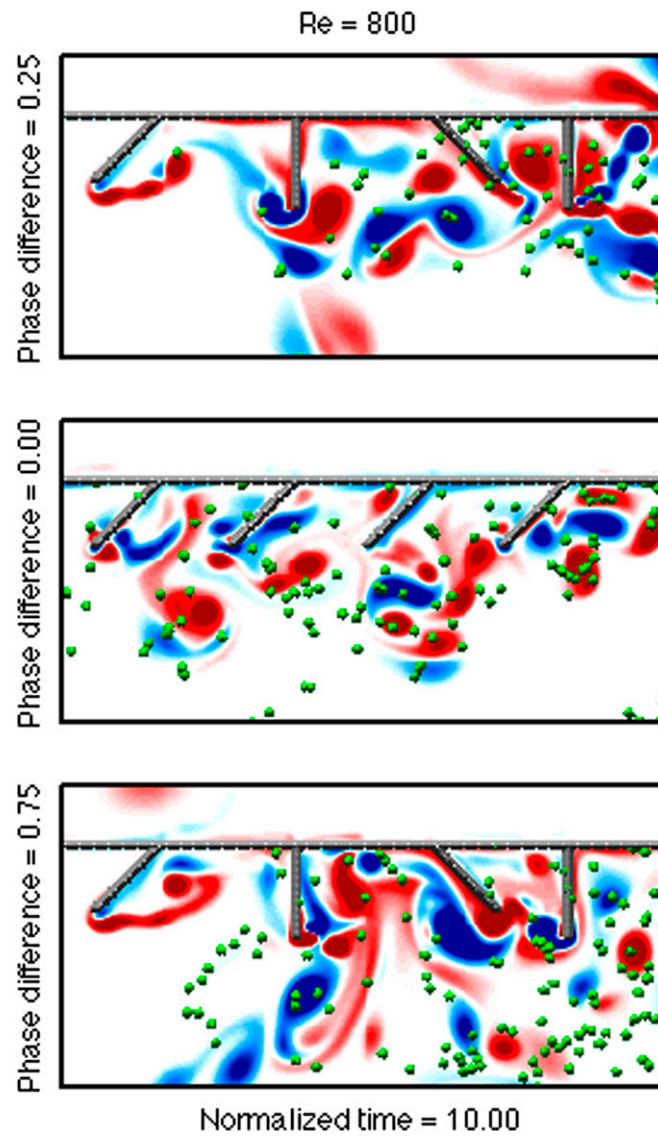
Movie S1. Flow field under three different stroke patterns at $Re = 50$. The time is normalized by the period of stroke. Free-flowing tracers shown as green dots are introduced at the end of the fifth stroke period. The vorticity of the flow field is shown in red–white–blue color (red denotes positive vorticity, and blue denotes negative vorticity). The natural tail-to-head metachronal wave (0.25 phase difference) is the most effective rhythm among the three stroke patterns in moving tracers toward the tail direction.

[Movie S1](#)



Movie S2. Flow field under three different stroke patterns at $Re = 200$. Variables and notations are defined in the same way as in [Movie S1](#).

[Movie S2](#)



Movie S3. Flow field under three different stroke patterns at $Re = 800$. Variables and notations are defined in the same way as in [Movie S1](#).

[Movie S3](#)